The Pennsylvania State University

The Graduate School

Eberly College of Science

TRANSLATIONAL AND ROTATIONAL DIFFUSION IN IONIC LIQUIDS THROUGH NMR SPECTROSCOPY

A Thesis in

Chemistry

by

Michael Shadeck

Submitted in Partial Fulfillment

of the Requirements

for the Degree of

Master of Science

August 2015

The thesis of Michael Shadeck was reviewed and approved* by the following:

Mark P. Maroncelli

Distinguished Professor of Chemistry

Associate Head for Undergraduate Education in Chemistry

Thesis Adviser

Karl T. Mueller

Professor of Chemistry

William G. Noid

Associate Professor of Chemistry

Michael A. Hickner

Associate Professor of Materials Science & Engineering, Chemical Engineering

Thomas E. Mallouk

Evan Pugh Professor of Chemistry

Head of the Department of Chemistry

*Signatures are on file in the Graduate School.

Abstract

In this work, translational and rotational diffusion in neat ionic liquids and dilute ionic liquid solutions were investigated using nuclear magnetic resonance (NMR) spectroscopy. Two distinct studies of translational diffusion were performed. The first focuses on solutions prepared in 1-alkyl-1-methylpyrrolidinium bis(trifluoromethylsulfonyl)imde ionic liquids ([Pr_{n1}][Tf_2N], *n*=3,4, and10) with quasi-spherical solutes, such as methane, ammonium, and tetramethylsilane. The second study entails measurement of self-diffusion coefficients in homologous series of neat ionic liquids: 1-alkyl-3-methylimidazolium bis(trifluoromethanesulfonyl)imide, [$C_nC_1$im][Tf_2N] and [(n-2)m$C_{n-1}C_1$im][Tf_2N] n = 3, 4, 5, 6, 7. The majority of the measurements of translational diffusion were carried out using a Bruker AV-III-850 NMR spectrometer with a Diff-30 probe with triple axis gradients using a longitudinal-eddy-current delay stimulated echo NMR pulse sequence.

The Stokes-Einstein (SE) model is a starting point for understanding the solute diffusion coefficients measured. While the SE model can often predict diffusion coefficients that are close to experimental values, there are several factors that can lead to deviations. The primary simplification of this model is to treat the solvent as a structureless continuum, thereby implicitly assuming that the solute is much larger than the size of the solvent molecules. Since ionic liquids are typically larger than conventional solvents, deviations from SE predictions are commonly observed for smaller solutes translating in ionic liquids. In addition to size, intermolecular interactions between the solute and solvent hinder the diffusion, leading to deviations. In the first translational diffusion study, charged and uncharged quasi-spherical solutes with various sizes were chosen to better understand deviations from SE predictions. By selecting these types of probes, shape effects are minimized and any deviation would be attributed to the fiction coefficient of the solute. The data collected here were important in verifying the accuracy of molecular dynamics simulations of these same systems. These simulations were able to provide new insight into the mechanisms of diffusion of small neutral and charged solutes in ionic liquids.

Translational diffusion experiments were also performed on two series of neat ionic liquids which differed in either having a linear or branched alkyl chain on the cation. These

liquids were provided by the Quitevis group from Texas Tech University. From their findings, it was observed that ionic liquids with the same composition but different alkyl chain connectivity exhibited large deviations in viscosity at certain chain lengths, while other physical properties, such as density, remained consistent. The self-diffusion coefficients of the cations and anions of two homologous series of neat ionic liquids were investigated to determine if analogous behavior was observed when compared to the viscosity.

Rotational diffusion studies analyzed dilute solutions of p-xylene-d_{10} (pXy^0), 1,4-dimethylpyridinium-d_7 hexafluorophosphate ($DMPy^+$), and p-tolunitrile-d_7 ($CMBz^{\mu}$) in 1-butyl-3-methylimidazolium tetrafluoroborate ($[Im_{41}][BF_4]$). For rotational diffusion experiments, data were collected using the DPX-300 spectrometer with a broadband multinuclear probe in addition to the AV-III-850. The pulse sequence used in these experiments was the inversion recovery for deuterium.

Determining rotational correlation times, τ_c, from deuterium longitudinal relaxation, T_1, is often oversimplified to the point of inaccuracy as a result of assuming exponential relaxation of rotational correlations. Factors such as symmetry and structure lead to molecules possessing several unique rotations and thus rotational correlation functions will have much more complex functional forms. In a previous study, correlation times for the rotational dynamics of benzene in ionic liquids were studied by fitting NMR data with the aid of MD simulations, eliminating the need for simplification. In the present study, the same type of analysis was used to determine rotational correlation times for probes having similar size and shape, but very different solvent interactions. The goal was to investigate the effect intermolecular interactions have on rotational diffusion.

Table of Contents

List of Figures

List of Tables

Chapter 1. Introduction

1.1. Ionic Liquid Properties

Ionic liquids (ILs) are bulky salts with melting points below 100°C that possess several distinctive properties compared to conventional liquids. Some of these features include low vapor pressure, high thermal stability, high conductivity and moderate chemical inertness.[1-2] One of the other features of ionic liquids that has drawn much attention is the capability to tune the ionic liquid for the desired application. The most common example of such tuning is the exchange of certain cations and anions in order to obtain desired bulk properties, such as viscosity. Additionally, small changes such as adding an additional methylene bridge can cause significant change in bulk properties of the liquid. Because of all the possibilities ionic liquids have to offer, they are of considerable interest in the fields of synthesis, catalysis, separations and electrochemistry.[1-2] Ionic liquids are complex media significantly different from conventional solvents in that they are composed completely of ions. Most cations of common ionic liquids are charged, aromatic rings with substituent alkyl chains that vary in length. When the alkyl chains are sufficiently long (greater than 4 carbon atoms) the ionic and alkyl portions of the liquid tend to segregate, forming locally polar and nonpolar domains. Because of the two domains, distinct electrochemical environments are created and the presence is thought to be important in understanding their function as solvents. It is hypothesized that the nanostructure that results from these domains may enhance or inhibit solute diffusion depending on the polarity of the solute and conjugate domain that it resides. In order to further their applications in various fields of study, the properties of these liquids must be understood. To achieve this, investigation of translational and rotational diffusion of various solutes in ionic liquids, the self-diffusion of neat liquids and the factors that could influence such diffusion was done.

1.2. Motivation

The motivation of this study was to investigate translational and rotational diffusion in ionic liquids in order to understand their behavior and the models that describe them through NMR spectroscopy. By relating factors such as solute-solvent interactions, viscosity, and ionic liquid structure to diffusion, the best suited ionic liquid can be selected for purposes that are reliant on diffusion. With respect to translational diffusion, the model used to predict solute diffusion in ionic liquids tends to fail under certain conditions. By exploring various experimental parameters, we hope to elucidate conditions that give rise to anomalous behavior.

1.3. Alternative Techniques

1.3.1 Translational Diffusion

Nuclear magnetic resonance spectroscopy (NMR) is a technique that can provide diverse information about a desired system. Among the information that NMR can provide, one that is often overlooked is translational diffusion coefficients. There are several other methods for determining diffusion coefficients other than NMR, the most common being electrochemical experiments. Based upon the system of interest, each type of measurement offers several advantages.

1.3.1.1. Electrochemical Methods

Among the realm of electrochemical techniques used to determine diffusion data, there are several features that must be accounted for.[2a] Due to the large viscosity of the ionic liquids, the diffusion coefficients of solutes are predicted to be significantly slower than those in conventional solvents. As a result, the experiment must be designed with this behavior in mind, most often in relation to the rate in which the potential is scanned.[3] Another condition that must be met is the analytes of interest must be redox active in order to probe electrochemical changes. Because of this requirement, analytes of interest are limited compared to the possibilities that can be analyzed with NMR. Additionally, because the solutes must be redox active, there are certain solvation effects that must be taken into consideration. In typical electrochemical experiments, conventional solvents are used, which inherently simplifies the analysis for the forward and reverse reaction due to common solvation between the neutral and oxidized/reduced species; it is

assumed the oxidized and reduced species will have similar diffusion coefficients.[3] Since one component of a redox reaction is a charged species, the solvation by the ionic liquid will be very different compared to the neutral counterpart. The charged species will possess an "ionic solvation" which will result in an increased hydrodynamic radius of the solute, significantly retarding the diffusion. Because of this solvation, the assumption that the oxidized and reduced species will have comparable diffusion coefficients fails.[3]

One technique that is used to probe diffusion coefficients of solutes in ionic liquids is potential step chronoamperometry. The basic principle of this technique is that current is monitored as a function of time as the potential is stepped over values of no current to oxidation/reduction. An advantage of chronoamperometry over other techniques is that it can simultaneously measure the diffusion coefficient and concentration of the probe and its redox counterpart.[3c-f] Additionally, steady-state conditions are not necessary for these measurements, which is advantageous since achieving such conditions is very slow for ionic liquid systems. To obtain the value of the diffusion coefficient for the forward reaction, the current-response data is fit to a set of equations, traditionally the Shoup and Szabo equations.[3g] On the other hand, the processing for the reverse step is not as facile as the forward step.

Cyclic voltammetry is another electrochemical technique that is often used to obtain diffusion data. Rather than current being measured as a function of time, this technique monitors current as a function of potential. In short, the potential of an electrode is ramped at a constant rate and the current is monitored as the voltage changes. After some time, there will be a maximum in the current, indicating the oxidation or reduction potential. Once that maximum current value is reached, the potential is ramped equally in magnitude but opposite in direction to the initial potential value. An advantage of being able to observe the redox potentials is that is it possible to identify complications that may occur within the reaction or complications with the electrode, information that chronoamperometry cannot provide.[3a-c] However, despite this advantage, there are several drawbacks to using this technique, specifically related to the rate in which the potential is ramped. In a study by Evans, *et. al.* on 1-alkyl-3-methylimidazolium bis(trifluoromethanesulfonyl)imide ionic liquids, several values of potential scan rates were tested and diffusion coefficients at each rate were compared.[3c] At a rate of 200 mV/s, peak shape behavior was obtained, representing transient conditions. It was not until the potential rate was

decreased to 5 mV/s until steady state responses were observed. Given the order of magnitude for diffusion coefficients in ionic liquids and the electrode parameters, steady state conditions should occur at a scan rate of 6.5 mV/s. Since the electrode specifications used for this calculation are often used in electrochemical experiments, the experimentally practical scan rate falls in between transient and steady state conditions, making diffusion coefficient extraction complicated. Because of this ambiguity in redox rates, cyclic voltammetry is often not a very popular method for determining diffusion coefficients.[3a-c] To remedy this, larger electrodes could be used, but in turn this would significantly increase the cost and duration of the experiments, which is unfavorable.

A third technique employed to quantify translational diffusion is scanning electrochemical microscopy. In summary, an electrode tip is scanned across the surface of the system and the steady state current is monitored as a function as of the tip-surface distance. As mentioned previously, a major drawback of most electrochemical techniques is the inefficiency of being able to detect the diffusion coefficient the oxidized and reduced compound because of the difference in solvation between redox species. Furthermore, inequalities in the diffusion coefficients cause anomalies in the current of the system which in turn causes erroneous data.[3a-c] While this is often problematic in the aforementioned techniques, transient mode scanning electrochemical microscopy takes advantage of this difference and allows for both diffusion coefficients to be determined.[3a, b] Despite this advantage, there are drawbacks to this technique, specifically preliminary measurements need to be performed in conventional solvents, and that steady state data is rather obsolete due to the easily misinterpreted data from using a viscous solvent like ionic liquids.

1.3.2. Rotational Diffusion

Analogous to translational diffusion, NMR is not the most obvious technique of probing rotational diffusion in molecules. The more common method used by researchers to obtain information about rotation is fluorescence anisotropy. There have been several research groups that used fluorescence anisotropy measurements to yield rotational dynamics in ionic liquid systems.[4] In order to perform this type of analysis, a fluorescent probe is subjected to polarized light. Upon an excitation event, the electron density within the molecule will relocate, yielding the excited state of the molecule. The most important feature to this experiment is the transition

dipole moment; only the molecules whose transition dipole moments that are aligned with the electric field of the polarized light will become excited, creating an anisotropic distribution of the transition dipole moment. If the molecules in the sample do not have enough time to rotate before relaxing, the transition dipole moments of the molecules will remain anisotropically distributed, and the light emitted by relaxation will retain the sample polarization as the excitation. On the other hand, if the molecules are able to rotate before relaxation, the anisotropy of the transition dipole moments will decay, as will the polarization of the light emitted. In order to obtain information about the rotation of the molecules, specific polarizations of the fluorescence relaxation are compared to the incident polarization, and any changes can be attributed to the rotational diffusion of the molecule.

The primary advantage of using this technique is obtaining time resolved data that describes the entire rotation that is probed. Due to the lack of time resolution within NMR experiments, anisotropy measurements are considered to be more advantageous with this respect. However, despite this paramount advantage, there are indeed several drawbacks to this method. In order to determine the decay in anisotropy, the molecule must rotate so that the transition dipole moment axis is changing. If a molecular rotation does not change the direction of the dipole moment axis, that particular rotation will be undetectable. Additionally, this technique is only limited to the realm of fluorescent probes whose rotations are faster than the lifetime of excitation.

In addition to fluorescence anisotropy, electron paramagnetic resonance spectroscopy (EPR) has also been used to determine rotational diffusion.[4c, d] This technique is similar to NMR techniques, but instead of nuclear spins, electron spins are excited. Analytes that are used in EPR measurements are limited to paramagnetic materials, which is a major drawback of this method. In addition to this, EPR measurements are not as advantageous compared to NMR measurements due to the faster relaxations of electrons, larger frequencies of the instruments, and larger linewidths within the spectra. Since NMR experiments do not have the same limitations as EPR measurements, EPR is typically not used in determining rotational diffusion information.

Chapter 2. Experimental Theory

2.1. Translational Diffusion

2.1.1. Spin Echo

Diffusion coefficients of analytes are most often measured through pulsed field gradient nuclear magnetic resonance spectroscopy (PFG-NMR). In order to understand such measurements, the spin echo experiment must first be understood. In the presence of an external magnetic field, the magnetic moment of a nucleus will precess at a particular frequency, known as the Larmor frequency, according to Eq. 2.1.[5]

$$\omega_0 = -\gamma B \qquad 2.1$$

In the equation above, γ is the gyromagnetic ratio of the nucleus of interest, and B is the magnetic field at the location of the particle. There are two types of magnetic fields that result in different nuclei in a sample precessing at different frequencies. The first comes from the microscopic magnetic fields that are caused by the local chemical environment of the spin. These microscopic magnetic fields are what give rise to different chemical shifts determined in many basic NMR experiments. In contrast, the macroscopic magnetic field, also known as the external magnetic field of the instrument, is present over the entire volume of the sample. Inhomogeneities in this external magnetic field give rise to imperfections in an NMR spectrum, such as peak broadening. In most experiments, it is desired to have the external magnetic field be homogeneous to avoid such imperfections.

A significant advantage of the spin echo experiment is that it does not require the external magnetic field to be homogeneous. This is made possible by the introduction of a π_x (180°) pulse, as seen in Figure 2.1.[5]

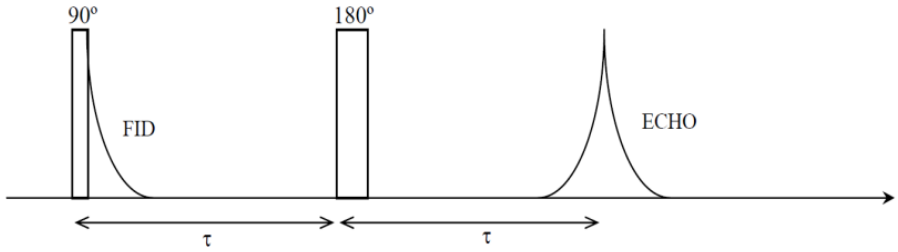

Figure 2.1. Basic Spin Echo pulse sequence.

After the $(\pi/2)_x$ (90°) pulse, the net magnetization will lie along the negative y-axis and will begin to precess. Due to the inhomogeneous external magnetic field, there will be varying field strengths throughout the volume of the sample. Spins located in magnetic fields of different strengths will result in a variation of Larmor frequencies, for example larger magnetic fields will result in faster precession, while smaller magnetic fields yield slower precession. The Larmor frequency is therefore dependent on the spatial region within the sample, and there is a distribution of magnetization vectors with varying frequencies. This variation in frequencies is known as dephasing, which is represented in Figure 2.2.[5]

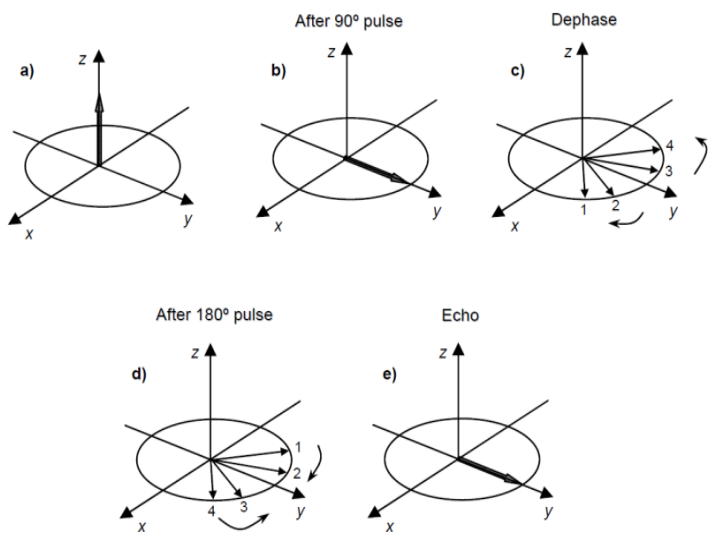

Figure 2.2. The net magnetization in the Spin Echo pulse sequence at (a) equilibrium (b) following the 90° pulse (c) dephasing of the magnetization (d) dephasing following the 180° pulse (e) the echo signal.

From the dephasing, the net magnetization is eliminated, and there is a loss of signal. Upon the π_x pulse, all individual magnetization vectors associated with each Larmor frequency are rotated about the x-axis while retaining their precessional frequencies. As a result, the faster and slower-precessing spins refocus simultaneously along the positive y-axis, giving rise to an echo signal.

2.1.2. Pulsed Field Gradient NMR

One of the caveats of the spin echo experiment is that in order to have perfect refocusing, the precession after the$(\pi/2)_x$ pulse must exactly cancel the precession after the π_x pulse. If the precession rate is altered, there will be a reduction in signal compared to the signal obtained after the $(\pi/2)_x$ pulse. One pathway the precessions would alter after the π_x pulse is due to the spins entering areas of new magnetic field strength. Because of this property, it is possible to detect molecular motion, in particular translational diffusion. In the case of pulsed field gradient (PFG) NMR, the basic principles of the spin echo are utilized, however there are slight variations implemented to yield information about translational motions of molecules.

The PFG experiment relies on being able to create controlled variations of magnetic field strength throughout the entire volume of the sample. This condition is met by introducing magnetic fields of different intensities along the z-axis, resulting in a gradient. Such gradients are introduced to the sample in the form of short pulses that break the homogeneity in a predictable way. By convention, the center of the sample is set to zero on the z-axis, meaning that spins above the center experience larger magnetic fields and below zero experience smaller magnetic fields. Because the inhomogeneities in the magnetic field are predictable, the spins are considered to be labeled as a function of position.[5]

The pulse sequence of the PFG experiment is demonstrated in Figure 2.3.[2a] Like spin echo, the experiment first begins with a $(\pi/2)_x$ pulse that results in traverse magnetization, which creates a signal. After some time, a gradient pulse is applied for a time δ/2, resulting in systematically varying precession rates as a function of *z*. These varying precession rates create a spiraling magnetization along the *z*-axis whose pitch depends upon the area of the gradient pulse. Once the gradient pulse ends, the labeled spins feel a homogeneous magnetic field and all spins precess at the same rate with retained dephasing. The π_x pulse causes the spins to rotate about the x-axis by 180°, giving rise to the mirror image of the spiral created after the first

gradient pulse. Once this mirror image is generated, the same gradient pulse is repeated, which result in the refocusing of the spins onto the positive *y*-axis, which creates the echo signal. If the nuclei did not change position between the first and second gradient pulse, the echo signal will have the same intensity as the initial signal observed. On the other hand, if the spins moved into a new region along the *z*-axis, the magnitude will decrease. Because of this, monitoring the attenuation of signal as a function of gradient strength allows one to measure diffusion along the *z*-axis.[5]

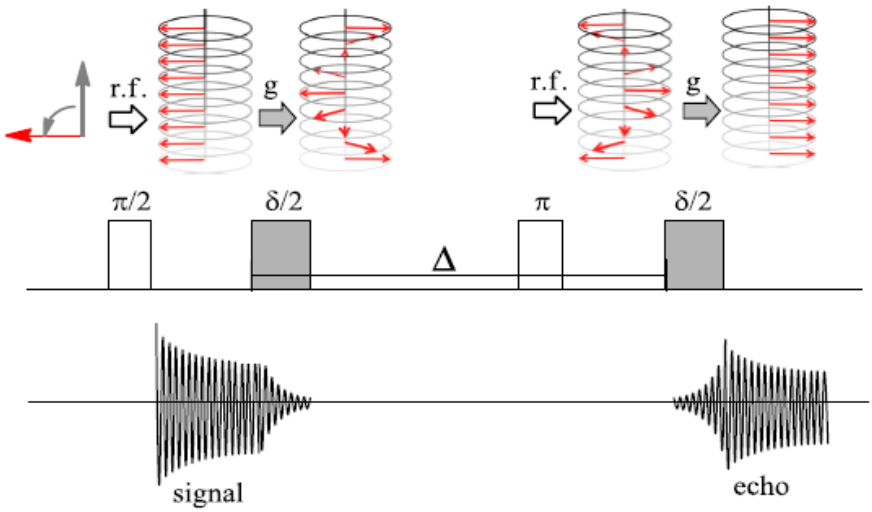

Figure 2.3. Simple Pulse Field Gradient (PFG) NMR pulse sequence. The radio frequency (r.f.) pulse is applied to a 90° or 180° rotation. A gradient (g) is applied along the *z*-axis for a duration of time (δ/2) to induce dephasing. The diffusion time (Δ) is the time between gradient pulses.

2.1.3. DOSY

PFG-NMR falls into the category of two dimensional experiments known as Diffusion-Ordered Spectroscopy (DOSY). A 1-D spectrum is collected at a set gradient strength, and the signal intensities are recorded. The strength of the gradient affects the dephasing of the net magnetic moment following the $(\pi/2)_x$ pulse; weaker gradients lead to less dephasing and stronger gradients leads to greater dephasing. In the case of weak gradients, the magnetic field does not significantly vary along the *z*-axis, meaning the solute would need to diffuse great distances to observe decay in signal, while strong gradients would only require short distances. The experiment is repeated over a range of gradient strengths, starting from low to high and

keeping the other parameters the same, ultimately creating a series of 1-D experiments with decaying signal intensity. By fitting the decay as a function of gradient strength, the diffusion coefficient can be determined.

2.2. Rotational Diffusion

2.2.1. The Deuteron

Determining the longitudinal relaxation time (T_1) of deuterium can yield useful information about the rotational dynamics of molecules in solution. Deuterons (and other spin-1 nuclei) possess a nuclear quadrupolar moment. This quadrupolar moment interacts with the electric field gradient (EFG, the second derivative of the electric potential) at the deuteron site. The direction of the major component of the EFG typically lies along the D-X bond of a molecule, and when a molecule rotates, the orientation of the bond changes and thus the EFG changes relative to the direction of the nuclear quadrupolar moment. If the frequency of EFG rotation relative to the nuclear quadrupolar moment contains components at the Larmor frequency of the deuteron, energy exchange between the nuclei and surroundings may occur and stimulate longitudinal relaxation.[6]

2.2.2. Rotational Time Correlation Functions and Shape Effects

Rotational motion is described in terms of rotational time correlation functions (tcfs) of unit vectors ($\hat{u}$) within molecules. In the case of NMR measurements, such tcfs take on the form:

$$C_{rot}^{(2)}(t) = \left\langle \tfrac{3}{2}[\hat{u}(0)\cdot\hat{u}(t)]^2 - \tfrac{1}{2} \right\rangle = \left\langle \tfrac{3}{2}\cos^2\theta(t) - \tfrac{1}{2} \right\rangle \qquad 2.2$$

The superscript "(2)" indicates a 2nd-order function of $\hat{u}(0)\cdot\hat{u}(t)$ and the brackets an ensemble average. For the case of rotational diffusion measured by NMR, the vector of interest is the direction of the EFG or the D-X bond direction and the angle θ it moves in time t. If the conditions have not changed, the correlation function is equal to 1. Once the conditions have changed to the point of the initial and final are unrelated, the correlation function is 0. A simple characterization of the time over which molecular orientation is preserved the correlation time (τ_{cor}), given by the integral of a rotational tcf:

$$\tau_{cor} = \int_0^\infty C_{rot}^{(2)}(t)dt \qquad 2.3$$

Depending on the molecular shape, different vectors within a molecule may give rise to distinct rotational tcfs. The simplest case is the spherical diffusor, in which the diffusion about any axis within the molecule is the same and rotational tcfs of any vector yield the form

$$C(t) = \exp(-t/\tau) \qquad 2.4$$

with the same correlation time τ. Most molecules are not spherical, and as a result the rotational tcfs are much more complicated. Rather than be modeled as a sphere, they are instead modeled by ellipsoids, which will have different speeds of rotation depending upon the axis of interest. In the case of a prolate ellipsoid, the EFG can lie along the major axis, one of the degenerate axes, or somewhere in between. If the EFG lies along a symmetry axis, rotation about that axis will not change the angle between the nuclear quadrupolar moment and the EFG, which means that particular rotation will be undetectable by NMR. However, if the EFG is not along a symmetry axis, molecular rotation about that symmetry axis will change the angle between the EFG and quadrupolar moment, rendering that rotation detectable.

2.2.3. Spectral Density Function and the Motional Narrowing Limit

The connection between longitudinal relaxation of a quadrupolar nucleus and rotational motion is given by[6]

$$T_1^{-1} = \frac{3\pi^2}{10}\left(\frac{e^2Qq}{h}\right)^2 \{j(\omega_0) + 4j(2\omega_0)\} \qquad 2.5$$

where Q is the nuclear quadrupolar moment, q is the electric field gradient at the nucleus and ω_0 is the Larmor frequency of the nucleus. The entire quantity, (e^2Qq/h) is known as the quadrupolar coupling constant (QCC), which expresses the relative strength of the coupling between the nuclear quadrupolar moment and the EFG. The other term, $j(\omega)$, is the spectral density function, the Fourier transform of the rotational tcf,

$$j(\omega) = \tfrac{1}{2}\int_{-\infty}^{\infty} C_{rot}^{(2)}(t)e^{-i\omega t}dt = \int_0^\infty C_{rot}^{(2)}(t)\cos(\omega t)dt \qquad 2.6$$

In the simplest case of a spherical diffuser, $j(\omega)$ becomes

$$j(\omega) = \frac{\tau}{1+(\omega\tau)^2} \qquad 2.7$$

In this case, substituting Eq. 2.6 into Eq. 2.4 provides

$$T_1^{-1} = \frac{3\pi^2}{10}\left(\frac{e^2Qq}{h}\right)^2\left\{\frac{\tau}{1+(\omega\tau)^2} + \frac{4\tau}{1+4(\omega\tau)^2}\right\} \qquad 2.8$$

T_1 is plotted as a function of τ for a fixed value of ω_0 in Figure. 2.4. If the QCC is known, one can determine the rotational correlation time from T_1.

Unfortunately, most rotational tcfs are not single exponential functions and thus the connection between rotation time and T_1 is not as simple as Eq. 2.8 suggests. However, under the condition $\omega_0\tau_c \ll 1$, T_1 becomes independent of the detailed shape of $C_{rot}^{(2)}(t)$ or ω_0 (Figure 2.4). This condition is known as the extreme narrowing limit wherein the connection between T_1 and rotational correlation time is direct and simple:

$$T_1^{-1} = \frac{3\pi^2}{2}\left(\frac{e^2Qq}{h}\right)^2 \tau_c \qquad 2.9$$

To determine if the extreme narrowing limit applies, one must vary ω_0 and observe where the data converges and in this region τ_c is obtained very easily. If one is outside of this regime, it is impossible to determine τ_c without choosing a model for the rotational tcf. Varying ω_0 is not the only mechanism for reaching the extreme narrowing limit. One can vary the temperature as a means of varying τ_c in similar fashion to varying ω_0. At higher temperatures, molecules will rotate faster and τ_c will decrease. Since ω_0 is independent of temperature, the value of $\omega_0\tau_c$ will decrease upon heating the sample and τ_c can be determined for some higher temperatures.[7]

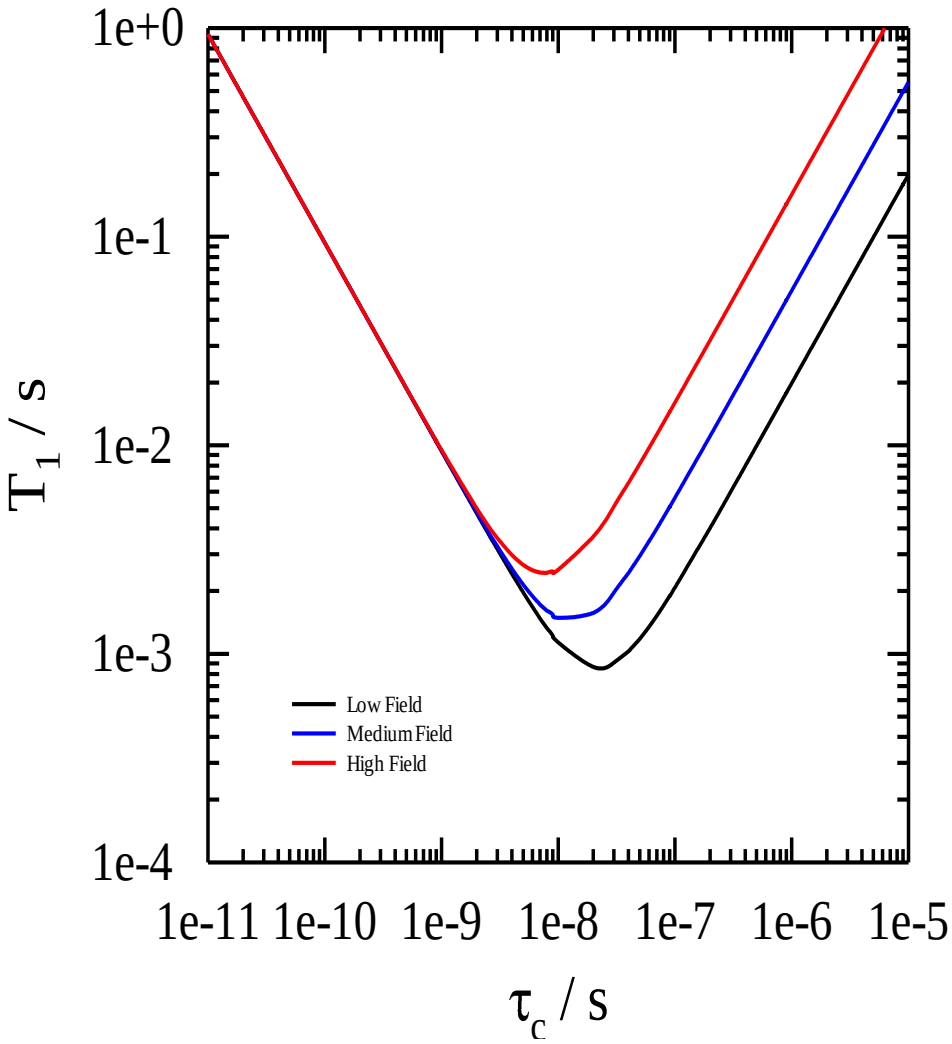

Figure 2.4. Longitudinal relaxation time (T_1) as a function of rotational correlation time (τ_c) and relative field strength. As the value of τ_c decreases, the field strength dependence vanishes.

2.2.4. Inversion Recovery

The longitudinal relaxation time is most accurately determined through the inversion-recovery pulse sequence (Figure 2.5).[2a] After a sample has reached equilibrium, the net magnetization of will be aligned with the external magnetic field (B_0). The pulse sequence begins with a 180° rotation as the result of a π r.f. pulse. After the magnetization has been inverted, it will evolve back toward its original direction. To monitor its progress and thus T_1, a $\pi/2$ r.f. pulse is applied after some delay time τ. This pulse interrupts the relaxation of the net magnetization and instantly put it in the *xy* plane. The strength of the net magnetic moment for a specific nucleus is reflected by the initial intensity of the free induction decay (fid). As the value of τ increases, the net magnetization has more time to relax towards equilibrium, thus bringing it closer to the initial positive intensity. By fitting the change in intensity of the fid with τ, the value of T_1 can be determined.[5]

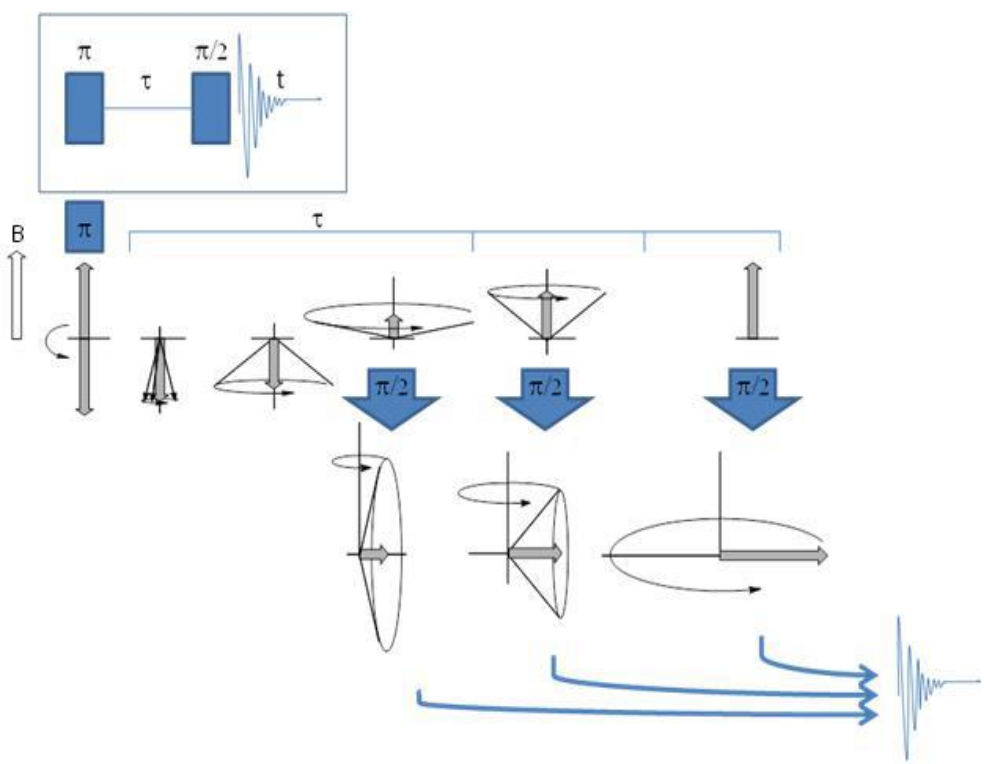

Figure 2.5. Inversion Recovery pulse sequence. The net magnetization is rotated 180° and after some delay (τ), a second 90° pulse is applied. Fitting the signal as a function of τ reveals the relaxation time.

Chapter 3. Experimental

3.1. Sample Preparation

Ionic liquids used in this study were synthesized by Gary Baker at the University of Missouri. Non-deuterated solutes used for the translational diffusion experiments were obtained from Sigma-Aldrich and were used as received. Deuterated solutes used for the rotational diffusion experiments were obtained from CDN Isotopes and were used as received. All ionic liquids used in this work were dried overnight in a scintillation vial attached to a vacuum having a pressure of approximately 0.01 Torr. To increase the rate of drying under vacuum, the samples were stirred and heated on a hotplate stirrer to approximately 60°C. After drying, the vials were capped and transferred to a positive pressure nitrogen glove box to prevent exposure to outside moisture. For preparation of dilute solutions, solutes were weighed outside the glove box and added to a pre-weighed and labeled scintillation vial with stir bar and cap. All solutions were prepared to concentrations of approximately 50 mM, which we have shown approximates infinite dilution conditions.[2a] At this concentration, solute-solute interactions are minimized and relevant solvent properties such as viscosity are within uncertainties of those of the neat solvent, but good signal-to-noise can be achieved in the NMR spectrum. The solutes were transferred to the glove box and the desired volume of dried ionic liquid solvent was delivered into the vial. Samples were capped and allowed to stir overnight to assure complete dissolution. For certain solutions, additional heating was required to assure complete mixing. In order to prevent contamination, capped samples were wrapped in parafilm and were placed on a hot plate stirrer outside the glove box overnight and returned to the glove box upon dissolution. To assure the solute had completely dissolved, the solutions were cooled for approximately one hour. Before preparing the samples, NMR tubes and long stem pipettes were baked to remove adsorbed water and transferred into the glove box. Further precautions were taken to prevent contamination of the sample by vacuum-sealing 5 mm economy 8” 200 MHz NMR tubes once the sample had been added. Approximately 600 μL of dried neat ionic liquid or dried solution was delivered to the NMR tube using a long stem pipette. To assure the sample reached the bottom, the tubes were tilted at a slight angle (roughly 45°) and delivered slowly.

3.2. Translational Diffusion Data Acquisition and Processing

Diffusion experiments were performed on a Bruker AV-III-850 NMR spectrometer with a Diff-30 probe with triple axis gradients using a longitudinal-eddy-current delay stimulated echo NMR pulse sequence. Earlier experiments were performed on a Bruker DRX-400 spectrometer, however the instrument became nonfunctional shortly thereafter. After some time, it was operational again, but the data acquired was not consistent with previous measurements taken on the same instrument or the 850. As a result, the data used in our analysis was based entirely on experiments performed on the AV-III-850. The samples used in this work were either neat ionic liquids or dilute solutes in ionic liquids without a lock solvent present, meaning all NMR measurements were performed unlocked. To assure the temperature stabilized at a target temperature, the samples were allowed to equilibrate in the spectrometer for 20-30 minutes. Following calibration, the instrument was tuned and shimmed for each new sample being measured and a 1-D proton spectrum was obtained to verify the quality of the shimming. Additionally, the rf pulse duration required for a $\pi/2$ rotation was calibrated. This was done by varying the duration of the rf pulse until a maximum peak intensity was obtained.

Exclusive to the diffusion experiment, the time delay between the two gradient pulses (Δ) and the duration of the gradient pulse (δ) must be optimized to assure acceptable peak area decay in the experiment. These values are directly related to the diffusion coefficient of interest and the gradient strength as seen in Eq. 3.1.[2a]

$$S(g) = S(0)\exp\left[D(\gamma\delta g)^2\left(\Delta - \frac{\delta}{3} - \frac{\tau}{2}\right)\right] \qquad 3.1$$

In this expression, S is the signal area, D is the diffusion coefficient of interest, γ is the gyromagnetic ratio of the nucleus of being probed, g is the gradient strength and τ is the time allowed for gradient recovery, which is at a default value of $2.0\text{x}10^{-4}$ s. In order to determine the diffusion coefficient, the initial gradient field strength of five percent of the maximum is applied to the sample and the signal area for the proton is acquired. The gradient strength is then incremented by ten percent and the experiment is repeated for a total of ten steps until a spectrum is collected at 95% of the maximum gradient strength. A plot of area as a function of gradient strength is generated, and D is determined from the fit of the exponential $S(g)$ curve.

To optimize the values of Δ and δ, preliminary values are assigned and the peaks of the spectra are observed over the entire range of gradient strength. In the beginning of the experiment, the gradient strength is small, and the peak area will be large. Since there are ten steps involved in the entire experiment, the optimal values of Δ and δ result in the amplitude of the peaks in the last step to be approximately ten percent of the amplitude of the first experiment. If the peak amplitude decays too quickly due to the value of Δ being too large, the signal at the larger gradient strengths will decay into the noise of the spectrum these points and will be useless. On the other hand, if the decay is too slow, not enough time for diffusion has been given and only the early stages of the decay will be captured, resulting in an unreliable fit. If the initial values of Δ and δ do not yield the desired decay, the values are changed and tested again. If the decay is very rapid or very slow, it is usually an indication that Δ should be altered as it is most sensitive to the diffusion rate of the analyte. Smaller changes in the decay can be fine-tuned by altering δ.

For this work, the values of cation diffusion coefficient were determined from ^{1}H spectra and values for anion diffusion coefficients were determined from ^{19}F spectra. All data were processed with the automated software provided with the instrument. Based upon the calibrated values previously mentioned, the diffusion coefficient was calculated by fitting the spectroscopic data to Eq. 3.1.

3.3. Rotational Diffusional Data Acquisition and Processing

For rotational diffusion experiments, data were collected using the DPX-300 spectrometer with a broadband multinuclear probe in addition to the AV-III-850. Following tuning and shimming, the deuterium filters were disconnected from the probe and the lock cable was removed, allowing the probe to be tuned to the deuterium frequency. Analogous to the diffusion experiment, the $\pi/2$ pulse duration must be calculated, only this time it will be for deuterium. With all the parameters set, inversion recovery experiments were performed over a designated temperature range and T_1 values were determined from automated software from Bruker.

3.4. Temperature Calibration

The AV-III-850 and DPX-300 were calibrated using a neat methanol sample for temperatures below 310 K and neat ethylene glycol for higher temperatures. Once the samples were equilibrated at the desired temperature for approximately 30 minutes, the probe was tuned and shimmed and 1D ^{1}H spectra for each temperature point were collected. As the temperature rises, the –OH resonance in both liquids shifts upfield relative to the $-CH_3$ or $–CH_2-$ resonance, which can be explained by the diminishing of hydrogen bonding interactions with temperature.[8] Thus, the difference between the two resonances reflects hydrogen bonding equilibrium and the temperature of the sample. Previous studies by Raidford et. al. collected measurements on high field instruments and compared the calculated temperatures to values determined from low field instruments, which showed minimal differences.[8] From this information, the temperatures calculated in this work were treated in a similar fashion, only the equations were scaled to the frequency of the spectrometer of interest. From this calculation, plots of calculated temperature (T_C) vs. applied temperature on the spectrometer (T_{APP}) were made for each instrument (Figures 3.1-3.4), where Eq. 3.2 and 3.3 respectively represent methanol and ethylene glycol as the temperature standard on the AV-III-850. Likewise, Eq. 3.4 and 3.5 represent methanol and ethylene glycol data collected on the DPX-300.

850 Temperature Calibrations

$$Methanol\text{:}\ T_C = 0.8227\, T_{APP} + 3.8495 \qquad 3.2$$

$$Ethylene\ Glycol\text{:}\ T_C = 1.2184\, T_{APP} - 12.561 \qquad 3.3$$

300 Temperature Calibrations

$$Methanol\text{:}\ T_C = 1.1338\, T_{APP} - 4.0472 \qquad 3.4$$

$$Ethylene\ Glycol\text{:}\ T_C = 1.2428\, T_{APP} - 7.4696 \qquad 3.5$$

Chapter 4. Translational Diffusion of Spherical Solutes in Ionic Liquids

4.1. Introduction

In this work, the diffusion coefficients (*D*) of several solutes dissolved in ionic liquids were determined experimentally as a means to explore deviations from the Stokes-Einstein (SE) hydrodynamic model. Previous studies have explored such deviations for planar aromatic molecules.[1-2] In the present work, the diffusion coefficients of quasi-spherical molecules were analyzed to understand how charge and size lead to deviations from SE predictions.

4.2. The Stokes-Einstein Model

Ionic liquids are complex media significantly different from conventional solvents in that they are composed completely of ions. Most cations of common ionic liquids are charged, aromatic rings with substituent alkyl chains that vary in length. When the alkyl chains are sufficiently long (greater than 4 carbon atoms) the ionic and alkyl portions of the liquid tend to segregate, forming locally polar and nonpolar domains. Because these two domains create distinct environments, their presence is thought to be important in understanding the function of ionic liquids as solvents. Unlike conventional solvents, ionic liquids can be tuned to have desired physical properties, such as viscosity, by combining different ions or by changing the length of the alkyl chain. Ionic liquids are intrinsically viscous which results in slow diffusion of solutes, a drawback when considering them as reaction media. Understanding how solutes diffuse will potentially help select an ionic liquid best suited to a given reaction or other purpose where solute transport is important.

The Stokes-Einstein (SE) equation is often used as a starting point for predicting the diffusion coefficient, *D*:

$$D = \frac{k_B T}{6\pi\eta R} \qquad 4.1$$

The diffusion coefficient is predicted to be inversely proportional to the translational friction coefficient, $\zeta = 6\pi\eta R$, which is assumed to be given by Stokes' Law for friction on a macroscopic sphere. The Stokes-Einstein equation assumes the diffusing solute can be approximated as a sphere with radius $R = (3V_{vdW}/4\pi)^{1/3}$ based on its van der Waals volume,

V_{vdW}, and the liquid is treated as a continuous fluid with viscosity η. Under the condition that the size of the solute is approximately the size of the solvent, SE predictions are often within a factor of 2 of experimentally determined values of D.[1-2]

The SE model is not always this accurate due to violation of several assumptions made in its derivation. As mentioned previously, Stokes friction was derived under the condition that the diffusing particle is a sphere. This condition is rarely met as most molecules are non-spherical. Some aspects of shape appeared to be relevant to departures from SE predictions in previous work from our group.[2a] Another important factor in the accuracy of SE predictions is the relative sizes of the solute and solvent molecules, which is measured here by the volume ratio of the solute to solvent, V_u/V_v. It has been determined[1-2] that D will approach SE predictions if the value of V_u/V_v is sufficiently large. However, when the volume ratio is less than one, SE predictions may be far from experimental values and diffusion is influenced by other factors, such as charge. In this chapter, the diffusion coefficients of several charged and uncharged quasi-spherical probes are measured by PFG-NMR and compared to SE predictions. Deviations from SE predictions are described in terms of the ratio $D_{SE}/D_{obs} = \zeta_{obs}/\zeta_{SE}$, to focus on how solute-solvent interactions lead to differences from simple hydrodynamic predictions.

Previous studies of solute diffusion performed by Anne Kaintz of the Maroncelli group were focused on determining the diffusion coefficients of a variety of aromatic solutes at near-infinite dilution in a similar series of ionic liquids, $[Pr_{n1}][Tf_2N]$ with n = 3, 4, 6, 8,10, as well as other assorted ionic liquids.[1-2] Solutes were selected to systemically alter properties such as size and shape to understand their effects upon solute diffusion rates. Dipolar aromatic and other solutes were used to observe the effect of solute polarity and to make comparison to literature data obtained electrochemically. Until the present study, all solutes measured by our group were planar.

4.3. Spherical Solute Analytes

For this work, a series of 1-alkyl-1-methylpyrrolidinium bis(trifluoromethylsulfonyl)imde ionic liquids ([Pr_{n1}][Tf_2N], *n*=3,4, and10) with varying alkyl chains were used as solvents. In contrast to our previous work, the solutes chosen were aimed to investigate the effects of size and charge on diffusion while retaining a quasi-spherical shape. To meet these conditions, the probes of interest were methane, tetramethylsilane (TMS), ammonium, tetraphenylmethane, tetraphenylsilane and tetraphenylphosphonium. All solutes were dissolved in [$Pr_{4,1}$][Tf_2N], but due to the insolubility of tetraphenylmethane and tetraphenylsilane in [$Pr_{10,1}$][Tf_2N], data was not collected. Methane and TMS were the only solutes dissolved in [$Pr_{3,1}$][Tf_2N].

4.3.1. Results and Discussion

To assess the agreement of experimental results to SE predictions, the friction ratio (ζ_{obs}/ζ_{SE}) was used (Figure 4.1). In previous studies in [Pr_{n1}][Tf_2N] solvents, it was observed that the friction ratio of an uncharged solute increases systemically with solute-to-solvent volume ratio,[1-2] which is congruent with data collected in the present study. As mentioned previously, SE predictions tend to diverge in the limit of small solute-to-solvent volume ratios, which can be observed when considering the methane data. Compared to the other neutral solutes, methane possesses a significantly smaller volume and friction ratio, resulting in the data to be sui generis. For charged solutes, trends in SE behavior are similar to uncharged solutes in the realm of large volume ratios, but significantly different when small. In the case of small volume ratios, it has been observed that the experimental friction coefficients are approximately twofold larger than SE predictions. This feature has been observed in previous studies using Li^+ as a tracer, conveying friction ratios even larger than values obtained for probes used in this work.[1-2] When a charged solute possesses a large volume ratio, as is the case for tetraphenylphosphonium, the friction coefficient approaches values that are comparable to neutral solutes of similar size and SE behavior is recovered.

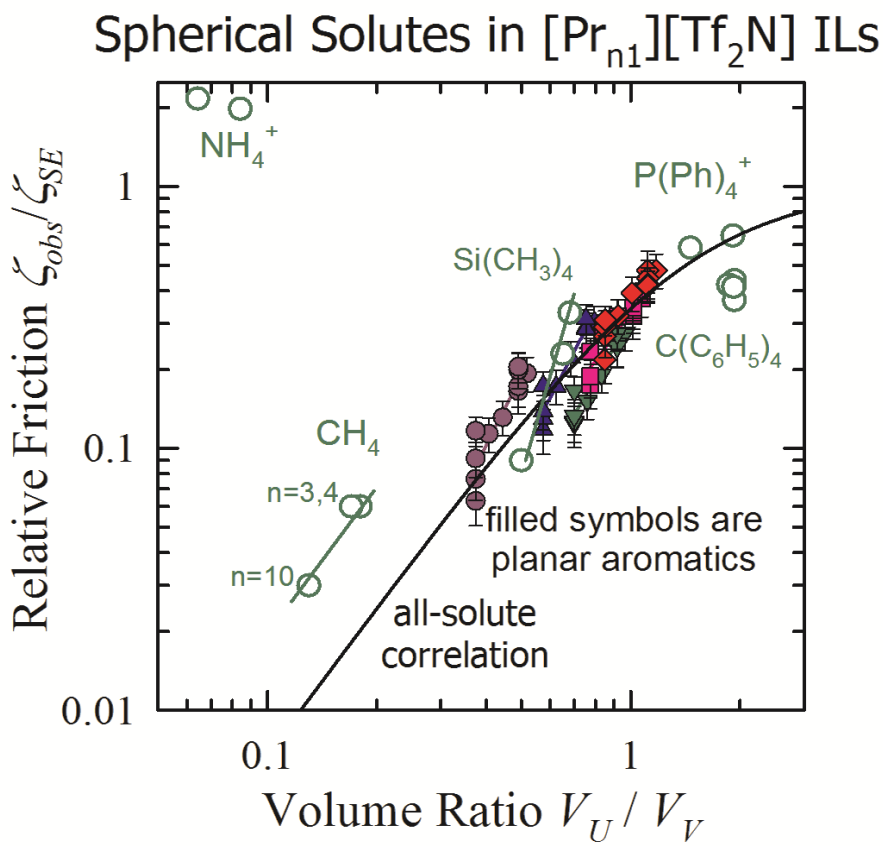

Figure 4.1. Neutral solutes with small volume ratios (CH_4) exhibit low relative friction, while small charged solutes (NH_4^+) experience large relative friction compared to SE predictions $\left(\frac{\zeta_{obs}}{\zeta_{SE}} = 1\right)$. This result is congruent with previous studies on size effects for charged and uncharged solutes. For methane, the enhanced diffusion is the result of enhanced mobility in regions of low polarity, while ammonium is significantly slowed by the enhanced hydrodynamic radius from strong interactions with the anion of the ionic liquid.

From the data collected here, it is clear that deviations from SE behavior are not exclusive to just size, the charge of the solute is also relevant. Most striking is the difference between methane and ammonium. These two solutes have nearly equal size, yet their friction ratios differ substantially. To further understand the molecular reasons responsible for this difference, MD simulations of CH_4 and NH_4^+ and several other solutes in [Pr_{41}][Tf_2N] performed by Araque et. al. of University of Iowa.[9] The alkyl chain in this ionic liquid is small enough that polar/nonpolar domain segregation is not possible, making this system a particularly simple case for examining the diffusion mechanism.

The simulated diffusion coefficients showed the same large differences between methane and ammonium observed experimentally (Figure 4.2). According to the simulations, methane experiences local regions of both high and low charge density. Since it does not couple strongly with the charged environments, the probe is free to diffuse throughout the entirety of the liquid and sample areas high in solvent-solvent friction (polar environments) and areas of low solvent-solvent friction (nonpolar environments). Polar environments are associated with a solute caging and slow diffusion, whereas the nonpolar regions enable translational jumps, resulting in motion much more rapid than small-step diffusion. In other words, methane diffuses slowly through the polar environments, but quickly through the low viscosity nonpolar environment with the net result that diffusion is much faster than SE predictions.

For ammonium, there is strong coupling with the solvent ions, particularly the anions, which prevents the probe from experiencing all regions of the liquid. In fact, what is actually observed is that a small solute becomes a source of electrostriction which hinders its motion in the polar environment. The solute is not diffusing independently, but is surrounded by anions, which can be thought of as increasing the hydrodynamic radius of the solute. The solute simply cannot be forced out of the charged region of the liquid, which enhances the local friction experienced by the probe compared to the bulk. As a result, diffusion is retarded, giving rise to a large friction ratio.

4.3.2. Summary and Conclusions

The diffusion coefficients of several quasi-spherical solutes were determined through PFG NMR experiments. Analogous to previous work, deviations from SE predictions were observed for probes possessing small volume ratios, further distinguished by their charge. In the case of the methane, the lack of charge resulted in faster diffusion while the high charge density of ammonium resulted in slower diffusion when compared to SE predictions. Simulation data were collected and compared to experimental results, yielding comparable diffusion coefficients. The trajectory of the probes from simulation concluded that methane diffusion is governed by solvent-solvent interactions while ammonium is highly influenced by solute-solvent interactions.

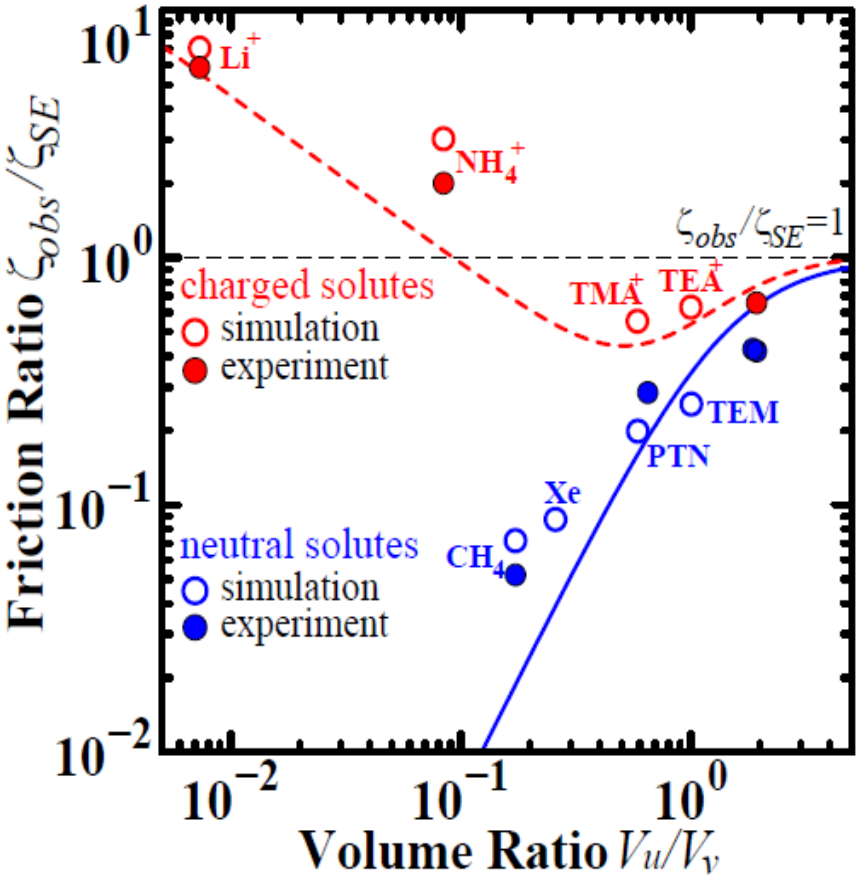

Figure 4.2. Simulated (empty circles) and experimental (filled circles) friction ratios as a function of volume ratio for charged (red) and neutral (blue) solutes agree reasonably well with one another. Experimental values were obtained by ^{1}H PFG-NMR measurements at 298 K, except for Li^+, which was obtained at 303 K in another study.[1] Simulated friction ratios were gathered at 400 K.

Chapter 5. Self-Diffusion of Branched vs. Linear Ionic Liquids

5.1. Introduction

The self-diffusion coefficients of several neat ionic liquids were determined. For ionic liquids with branched nonpolar tails, Quitevis and coworkers observed an unexpected pattern in viscosity at a certain chain length that is not present in the linear counterpart.[2b] Our goal was to determine if the diffusion coefficients of the constituent ions exhibited trends congruent to those of viscosity and provide a possible explanation as to why this may be occurring.

5.2. Ionic Liquids of Interest

Cations of several common ionic liquids are composed of both a charged, aromatic head group and a nonpolar tail. Very often the length of the alkyl portion of the cation is varied in order to alter the bulk properties of the liquid. At least within a homologous series of liquids, one finds that properties vary in a simple manner with chain length. Most data of this sort comes from ionic liquids having linear alkane substituents. However, there is not much information about ionic liquids with branched nonpolar tails and how this change in molecular structure affects bulk properties compared to their linear counterparts.

The Quitevis group at Texas Tech University performed several experiments on two series of linear and branched 1-alkyl-3-methylimidazolium bis(trifluoromethanesulfonyl)imide ionic liquids, $[C_nC_1im][Tf_2N]$ and $[(n\text{-}2)mC_{n\text{-}1}C_1im][Tf_2N]$ n = 3, 4, 5, 6, 7 (Figure 5.1). It was determined that branched/linear pairs of ionic liquids with the same number of alkyl carbons (n) have the same density (Figure 5.2), while the branched ionic liquids possess larger viscosities. Within the branched series, there is an anomalous increase in the viscosity when there are four alkyl carbons, as seen in the plot of viscosity vs. n (Figure 5.3). Based upon other experiments performed by Quitevis and coworkers, analogous behavior for the branched liquids is observed for other physical properties.

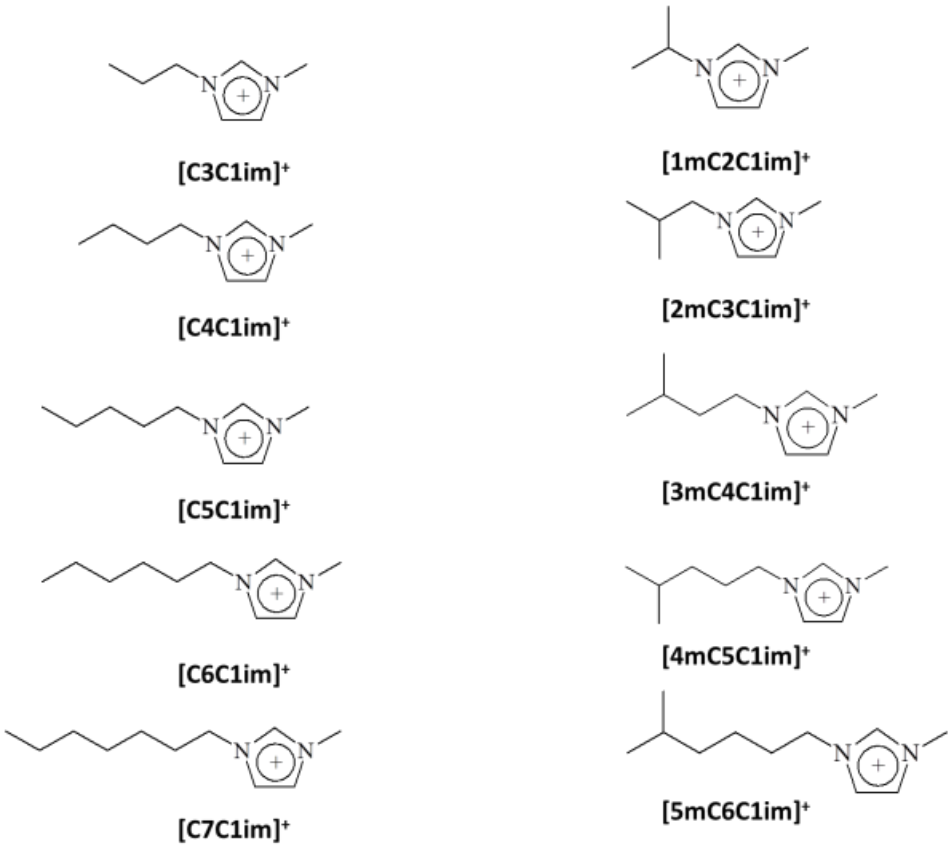

Figure 5.1. Linear and branched 1-alkyl-3-methylimidazolium bis(trifluoromethanesulfonyl)imide ionic liquids, $[C_nC_1im][Tf_2N]$ and $[(n\text{-}2)mC_{n\text{-}1}C_1im][Tf_2N]$ where n = 3, 4, 5, 6, 7

The present chapter concerns measuring the self-diffusion coefficients of the ions of both of these series of ionic liquids and comparing them according to alkyl chain length. The goal was to determine if the curious behavior shown by viscosities was also present in the ion diffusion coefficients. If the trends are consistent, it is suggestive that the unusual behavior caused by the details of alkane chain structure is also influencing the dynamics of the liquids. In order to test this hypothesis, we determined the self-diffusion coefficients of the cation and anion of each ionic liquid.

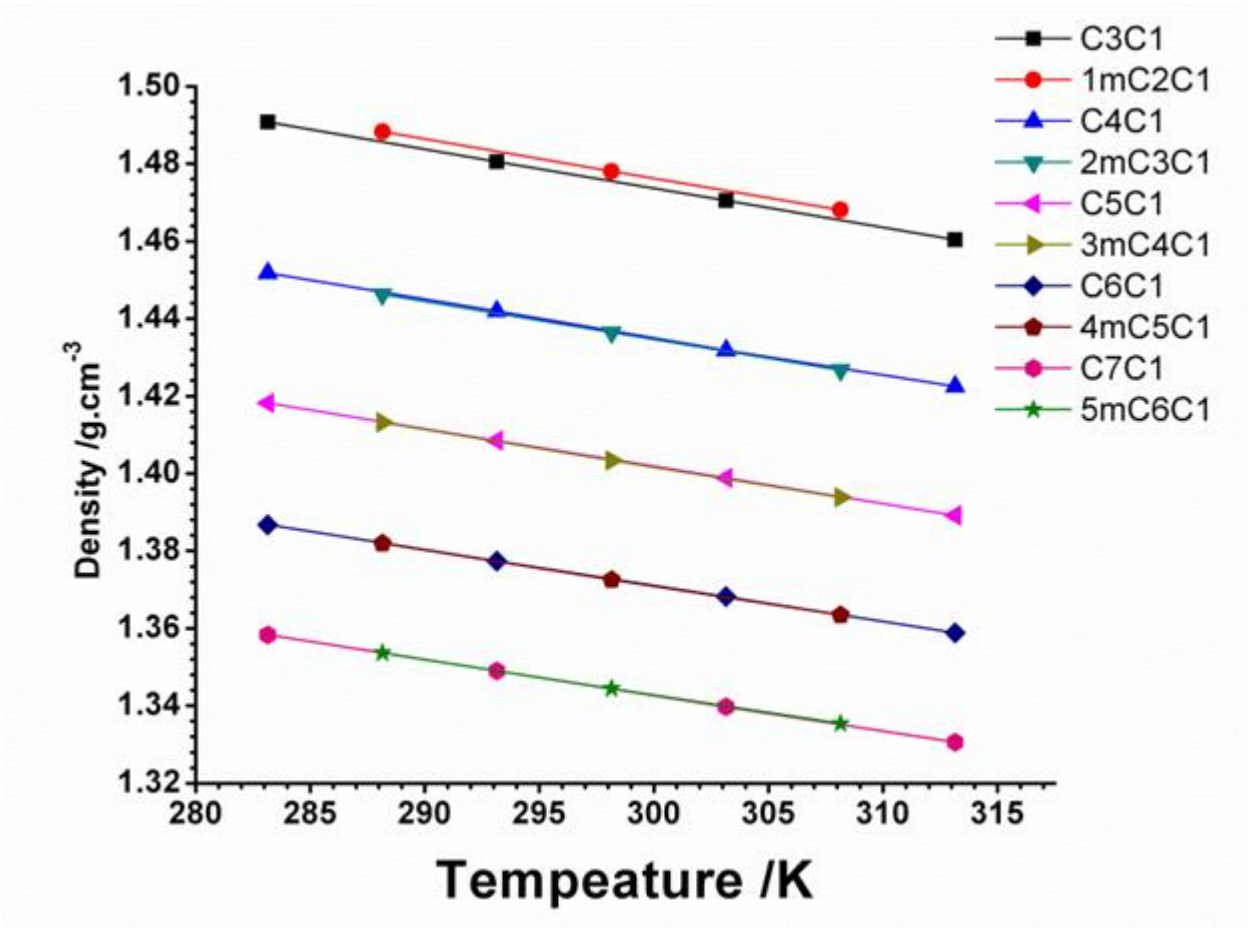

Figure 5.2. Densities of branched and linear ionic liquids of the same value of *n* possess similar densities. Unlike viscosity, there is not a deviation when *n* = 4.

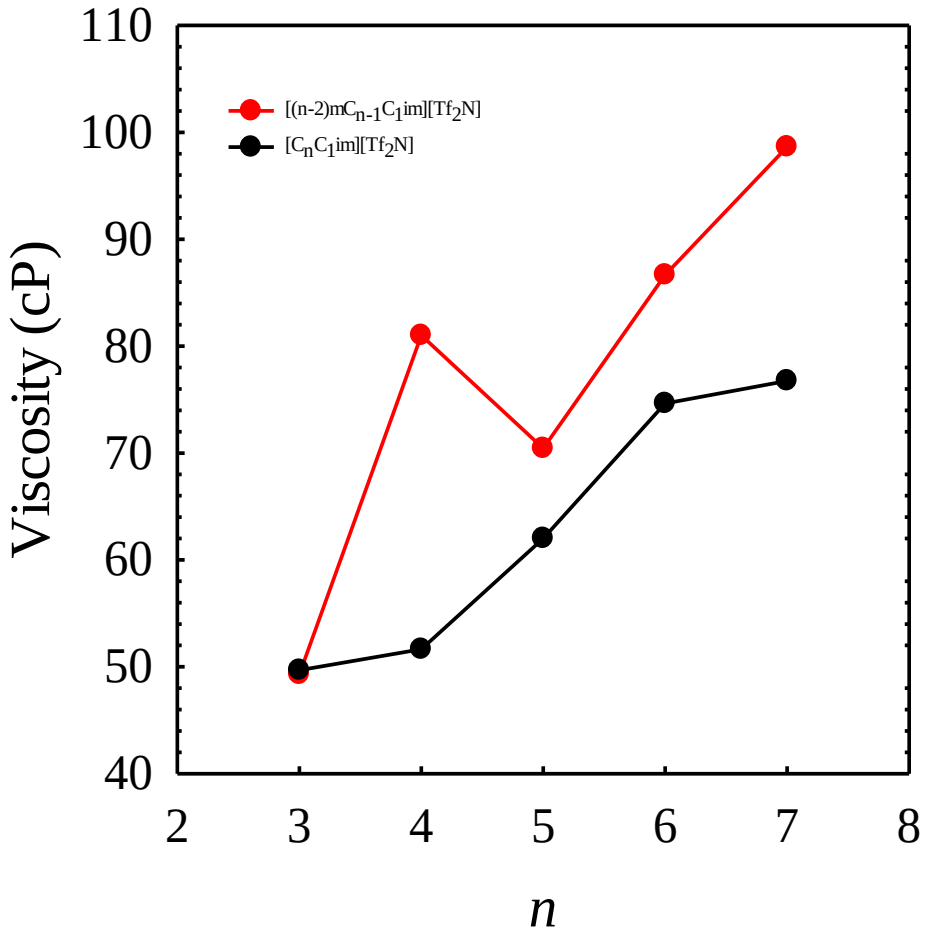

Figure 5.3. Bulk viscosity of $[C_nC_1im][Tf_2N]$ and $[(n\text{-}2)mC_{n\text{-}1}C_1im][Tf_2N]$ n = 3, 4, 5, 6, 7. A non-monotonic increase in viscosity as a function of n is observed for the $[(n\text{-}2)mC_{n\text{-}1}C_1im][Tf_2N]$ between $n=3$ and $n=5$.

5.3. Results and Discussion

5.3.1. Diffusion Data

Diffusion coefficients for each branched ionic liquid were first gathered at 298 K on the 400 MHz spectrometer. A non-monotonic dependence on *n* near *n*=4 was observed, consistent with the viscosity data previously collected. Temperature dependent measurements at 273, 283 and 313 K were additionally collected to determine the effect temperature would have on this trend (Figure 5.4). Within a single liquid, the diffusion coefficient increases as the temperature increases and viscosity decreases, a result that is expected from the SE model. At temperatures of 273, 283 and 298 K, the anomaly when *n*=4 is still discernible, however at 313 K, the diffusion coefficients for the *n*=4 and *n*=5 ionic liquid approach the same value.

In addition to the data collected on the 400, repeat trials were done on the 850 MHz spectrometer to test the consistency of the measurements. Analogous to the 400, the diffusion coefficients possessed a non-monotonic dependence on the alkyl chain length when measured on the 850. Comparing the values of the diffusion coefficients between the instruments resulted in an average difference of 19%, which is slightly higher than experimental uncertainties estimated in previous studies. A possible explanation for the deviations was inequivalent temperatures of the samples, indicating the need to collect repeat measurements on both instruments at the same temperature. Second and third trials collected on the 850 were performed at a calculated temperature of 297.5 K, compared to the first trial being collected at calculated 292 K. When the second and third trials were compared, a difference of 0.7% was observed, suggesting that data gathered on the 850 was reproducible under equivalent temperature conditions. Unfortunately, repeat measurements in the same fashion could not be obtained on the 400 due to maintenance issues. Because of the lack of repeat measurements on the 400, all data considered for this study comes from the second and third trials on the 850. The linear ionic liquid measurements were also measured on the 850 at the same temperature (297.5 K), yielding an average difference of 2.4%.

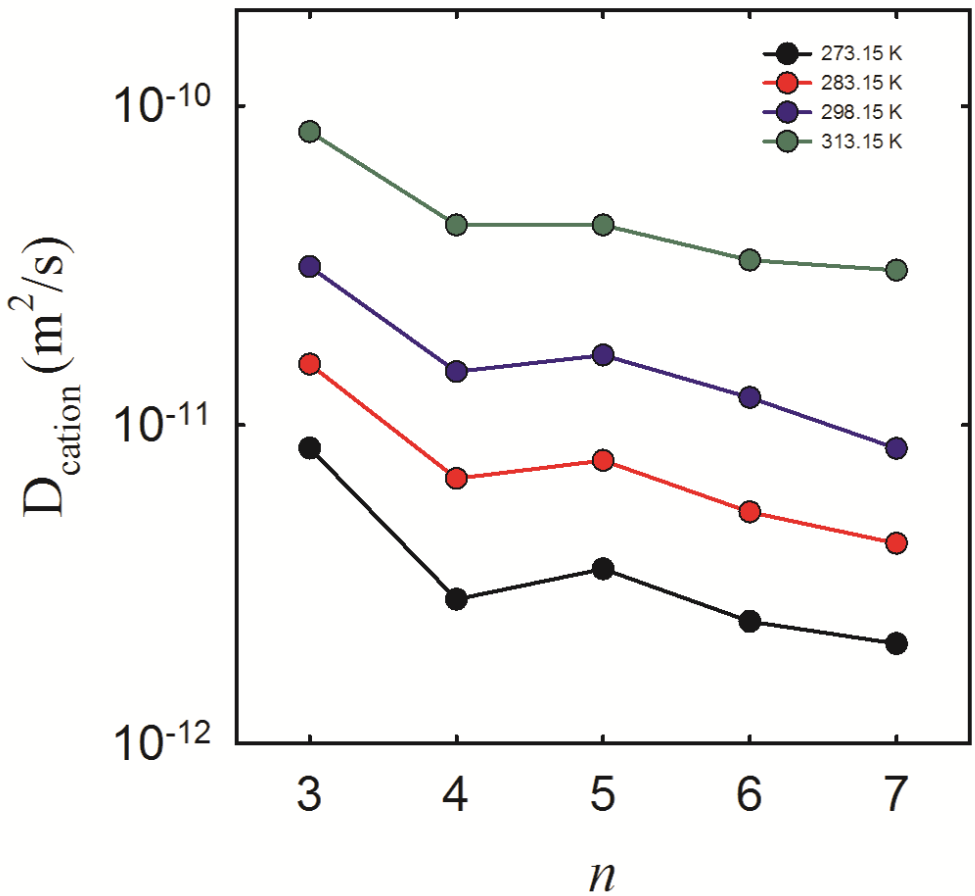

Figure 5.4. Within a single value of *n*, the cation diffusion coefficient (D_{cation}) measured on the 400 MHz spectrometer increased as the temperature was increased, a result that is expected from SE predictions. The same anomaly observed when $n = 4$ is still present as the temperature is increased, except at 313.15K, where the values at $n = 4$ and 5 approach the same value.

The average cation/anion diffusion coefficients and viscosity of the branched ionic liquids as a function of *n* are depicted in Figure 5.5 and the linear ionic liquids in Figure 5.6. As the alkyl-chain length increases, it is observed that the self-diffusion coefficient of the cations decreases. However, similar to the viscosity data, there exists an anomaly at n=4 for the diffusion coefficients for the branched ionic liquids, resulting in a non-monotonic trend with alkyl-chain length. Within the linear ionic liquids, both the diffusion coefficients and the viscosity vary monotonically as the length of the alkyl-chain increases. Similar behavior of the diffusion coefficients and the viscosity supports the Quitevis group's

hypothesis that alkyl chain branching mediates both the bulk properties and the dynamics of the liquids. On average, the diffusion coefficients of the branched cations are smaller than the linear cations, with an exception of *n*=5 and 7 and the values appear to converge. From this observation, it would suggest that at these chain lengths, the structure of the chain does not seem to impact the diffusion of the cation.

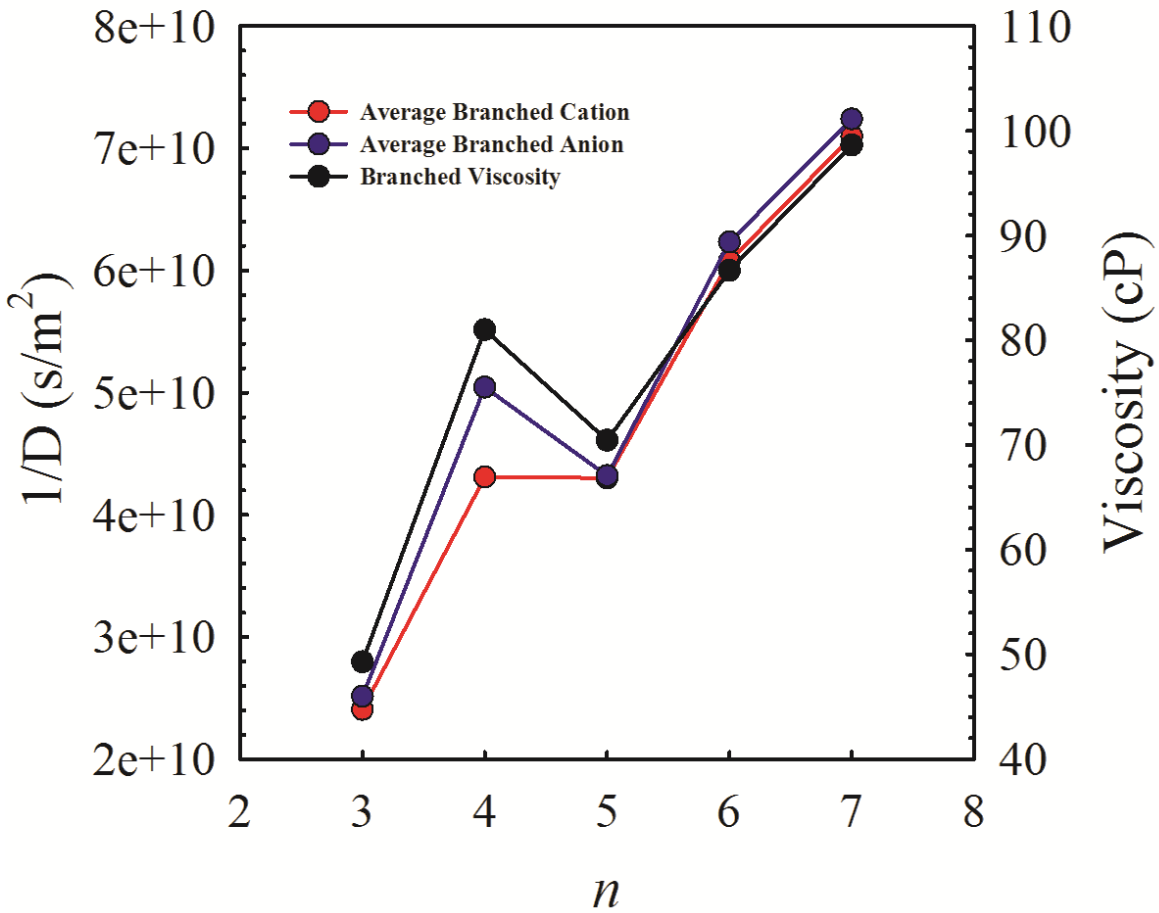

Figure 5.5. Comparison of the average diffusion coefficients for the branched cations and anions at 298K (red and blue , respectively) show similar behavior to their viscosities at 298 K. In the case of the branched series, an anomaly when *n* = 4 is observed in the diffusion coefficients that is comparable to the viscosity deviation. These observations support claims purported by the Quitevis group that the branching may affect dynamics of the ionic liquid.

So far, all results obtained have only measured the diffusion coefficient for cations of the ionic liquids and the behavior has been attributed to the structure of their nonpolar tails. However, little attention has been given to how the structure of the cation may influence anion diffusion. In order to determine if cationic structure exclusively influences cation diffusion, ^{19}F diffusion measurements were performed and the results were analyzed in a similar fashion. If the anion diffusion coefficients convey a similar dynamical anomaly as a function of alkyl-chain length, it is suggestive that cationic structure is dictating the dynamics of both ions

Comparing the anion self-diffusion coefficients and the bulk viscosity yielded results that were congruent to the behavior exhibited in the cation data (Figure 5.5 and Figure 5.6). In the case of the anions paired with the branched cations, the same deviation when n=4 was found, while anions paired with linear cations revealed the same monotonic dependence. Because of the comparable behavior between diffusion and viscosity is also observed in the anion measurements, it would suggest that the structure of the cation also dictates the diffusion of the anion. When comparing the values of the diffusion coefficients between the cations and anions within the same liquid, the cations are diffusing faster, on average, than the anions in the case of $n \leq 6$. When $n = 7$, the diffusion coefficient for both the branched and linear cation/anion pairs appear to converge to approximately the same value. For shorter lengths, it would seem that the alkyl-chain structure has some sort of effect on the interactions between the cation/anion pairs. These observations would suggest that once the alkyl-chain length approaches a certain length, the structure of the nonpolar tail does not have a distinguishable effect on the dynamics of either the cation or anion. If the interactions between the cations and anions are affected by the structure of the nonpolar tail, it is hypothesized that the dynamical anomaly seen could result from the packing of the ions within the liquid. In order to determine the packing of the ions, it was decided to examine ^{1}H and ^{19}F chemical shift values of these ionic liquids to see if there was any unique behavior, attributing it to structural/packing differences near n=4.

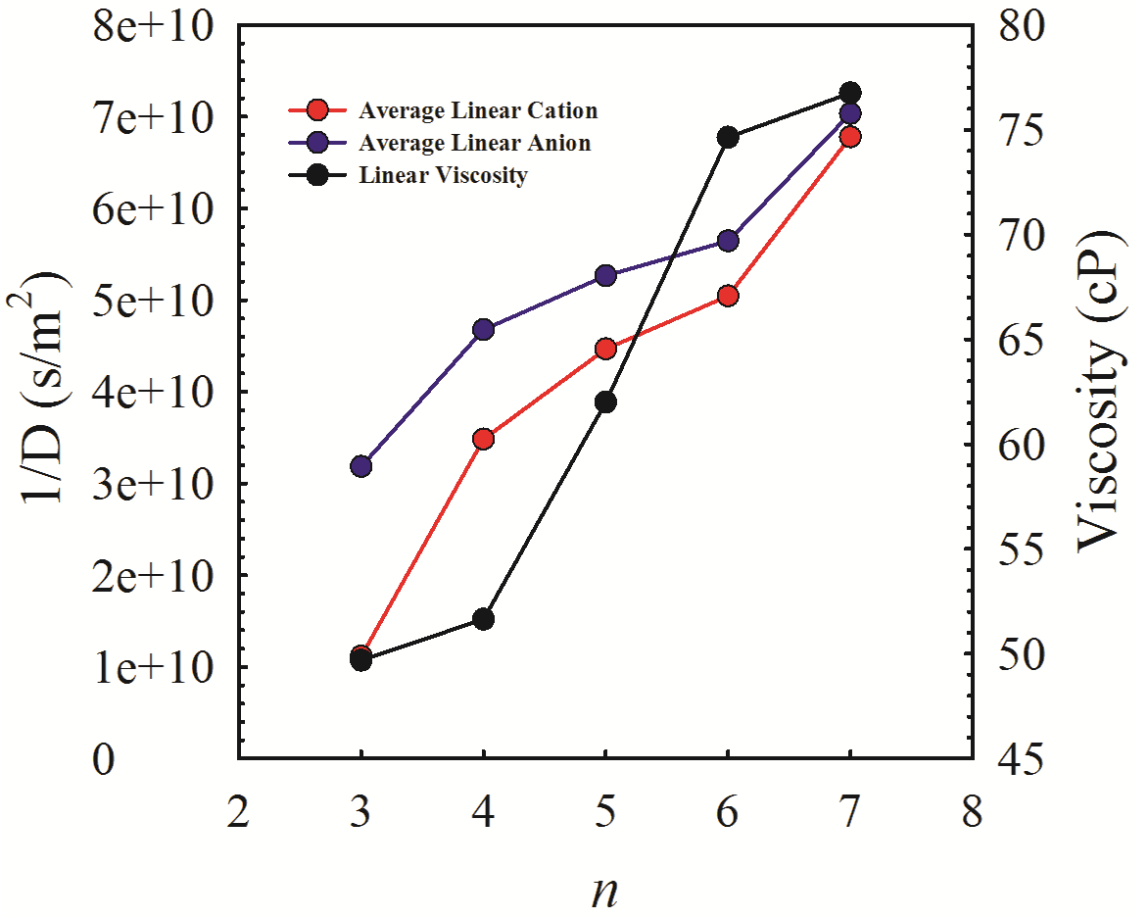

Figure 5.6. Linear cation and anion diffusion compared to its respective viscosity also shows congruent behavior. This observation suggests that not only does the branching affect the dynamics of the cation, but the anion is sensitive to it as well.

5.3.2. Chemical Shift Data

Preliminary ^{1}H chemical shift data were collected on the DRX-400, however the instrument became nonfunctional shortly after measurements were started. The AV-360 was chosen as an alternative after verifying that the chemical shift values obtained between instruments were consistent. Therefore, all chemical shift data reported were collected on the latter instrument. The protons of interest are labeled according to Figure 5.7.

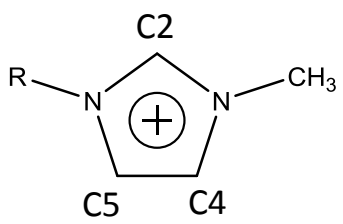

Figure 5.7. The skeletal structure of an imidazolium cation. Protons analyzed in the chemical shift study were on carbons 2, 4, 5, and the methyl group on the ring.

All chemical shift data and figures can be found in the Appendix. The chemical shifts for the branched ionic liquids display distinct dependences on *n* for the C2 proton and C5 proton, while the C4 and terminal methyl protons are similar to one another. In the case of the linear series, the patterns of all of the chemical shifts versus *n* are the same. At *n* = 4, there is a decrease in the chemical shift value but then increases from *n* = 5 and longer. In the case of the ^{19}F chemical shifts, the branched series again yielded different pattern from the linear series. In the case of the branched series, there appears to be a steady increase in chemical shift as the chain length becomes larger, a trend that is synonymous with the C2 proton data. On the other hand, in the linear series, the ^{19}F chemical shifts exhibit the same behavior common to all protons, the chemical shift at *n* = 4 is lower than expected based on the trend of the other members of the series.

It was hypothesized that this occurrence at *n* = 4 could be the result of some sort of subtle structural/packing effect in the liquid. To test whether this was the case, we measured the chemical shifts of 50 mM ionic liquid in DMSO-d solutions with a trace amount of TMS as an internal standard. Rather than the entire series performed again, we chose to analyze the *n* = 3, 4 and 5 liquids to see if analogous results were obtained.

The dilute solution experiments yielded very different patterns in chemical shift as a function of *n*. For the C2 proton of the branched, the behavior observed in the neat liquid is not seen in the dilute samples, that is the chemical shift drops at $n = 4$ and then increases again. Conversely, the linear samples do not seem to contain this anomaly at the same location, which is also opposite of what is observed in the neat liquids. For the branched liquids, the proton on C4 seems to follow the same pattern as the neat sample because there is a slight increase at $n = 4$ and then decrease at $n = 5$. In the linear samples, a similar pattern in the dilute samples are observed but with a larger magnitude. However, what is very peculiar about this result is that it is such a drastic change from what is seen in the neat linear sample; rather than decreasing when $n = 4$, there is a sharp increase. The C5 proton for both types of ionic liquids contain analogous patterns for the neat samples, specifically a decrease at $n = 4$ and then a jump back up when *n* reaches 5.

The chemical shift is a reflection of the chemical environment experienced by the proton. At high electron density, the protons will be shielded from the external magnetic field and will have a small chemical shift value while a large chemical shift means reduced electron density. In the case of the neat branched ionic liquids, it would seem that the ring protons are in fact experiencing new chemical environments as the alkyl chain length increases, yet the change in environments do not appear to be consistent for each proton, evident by the different trends for each proton. In contrast, the same patterns are observed in the neat linear chain liquids, implying that the change in chemical environment is more consistent. For both liquids, the most pronounced change occurs when $n = 4$, excluding the C2 proton in the branched liquid. When the chemical shift increases sharply, this is suggestive that the proton becomes more deshielded as the alkyl chain increases. In the case of branched C4 and methyl protons on the ring, it is possible that the electron density experienced by the protons decreases as a possible result of the bulky alkyl tail becoming further away with chain length. Conversely, for all linear protons and the C5 proton of the branched, the substantial drop in chemical shift implies increased electron density, causing a shift upfield. In other words, it would seem that somehow the electron density is increasing around the site of these protons, a result that could manifest as a result of having an alkyl group in close proximity. Despite the hypotheses, none of the observations are conclusive to what is happening. At this point in time, we do not have any conclusions that can be rationalized on these data alone.

Chapter 6. Rotational Diffusion in Ionic Liquids

6.1. Introduction

The longitudinal relaxation times (T_1) of deuterons in rotational probes p-xylene-d_{10}, 1,4-dimethylpyridinium-d_7 hexafluorophosphate, and p-tolunitrile-d_7 dissolved in 1-butyl-3-methylimidazolium tetrafluoroborate were measured. The purpose for selecting these probes was to observe the effect of solute-solvent interactions on rotational correlation times (τ_c). By measuring the longitudinal relaxation time of each deuteron in the analyte and comparing the resulting rotation times with molecular dynamics (MD) simulations, we hope to determine the most simplistic yet accurate representation of the rotational correlation function of each unique rotation within the molecule. Furthermore, we want to investigate how intermolecular interactions affect rotational diffusion when dissolved in ionic liquids.

6.2. Determining the Rotational Correlation Function through NMR

Common analysis of rotational diffusion data draws a relationship between the longitudinal relaxation time, T_1, to the rotational correlation time, τ_c, assuming that the probe possesses a single exponential rotational time correlation function. A drawback of this assumption is that this functional form is only applicable to solutes with a high degree of symmetry, such as a sphere, such that only one diffusion coefficient suffices to describe all reorientation. For most molecules, this condition is unlikely, and therefore the relationship between T_1 and τ_c becomes more complex. Shape has a paramount effect on the number of rotational diffusion coefficients present within a molecule. In most cases, molecules are approximated by ellipsoids of varying symmetry. In the case of a symmetric ellipsoid, there will be two different diffusion coefficients if it is assumed that the vector of interest (EFG in the case of NMR) lies along the principal axis of symmetry. If the molecule is rotated about the principal axis, the rotation correlation function cannot relax, and thus a diffusion coefficient is not present. However, rotation about either of the degenerate axes will produce the same correlation function with the functional form of a single exponential decay, where $\tau = \frac{1}{6D_\perp}$.

$$C_r(t) = \exp(-6D_\perp t)$$

For the EFG lying along one of the degenerate axes, there is not a single rotation that defines the change in position of the vector. As a result, there will be a more complex correlation function to define its rotational motion, specifically a bi-exponential decay.

$$C_r(t) = 0.25\exp(-6D_\perp t) + 0.75\exp[-(2D_\perp + 4D_\parallel)t]$$

In a previous study performed by Anne Kaintz of the Maroncelli group, the rotational correlation functions of benzene-d_6 were determined through use of NMR measurements and MD simulations.[2a] Since the connection between T_1 and τ_c is not well understood,[2a] the goal of this prior study was to provide a better understanding of the connection between them, which would provide a standard protocol for determining correlation functions for future probes. For the present work, we wanted to represent the rotational relaxations found in three similarly structured probes with varying solute-solvent interactions in the simplest way.

6.3. Rotational Probes

For the present study, we wanted to compare probes that were similar in structure, yet possess different interactions with the solvent. By keeping a similar structure, rotations of certain axes will be closely related, thus any variations between the correlation functions can be attributed to the different types of solute-solvent interactions. To meet these criteria, we have selected p-xylene-d_{10} (pXy^0), 1,4-dimethylpyridinium-d_7 hexafluorophosphate ($DMPy^+$), and p-tolunitrile-d_7 ($CMBz^\mu$) as our molecules of interest (Figure 6.1). The probes were dissolved in 1-butyl-3-methylimidazolium tetrafluoroborate ($[Im_{41}][BF_4]$) to create 50 mM solutions in order to provide infinite dilution conditions. Due to the wide temperature window of the experiments, it is necessary to select a liquid that will remain a liquid over this window. Because of this requirement, $[Im_{41}][BF_4]$ was chosen as the solvent because it will remain liquid at low temperatures.[2a]

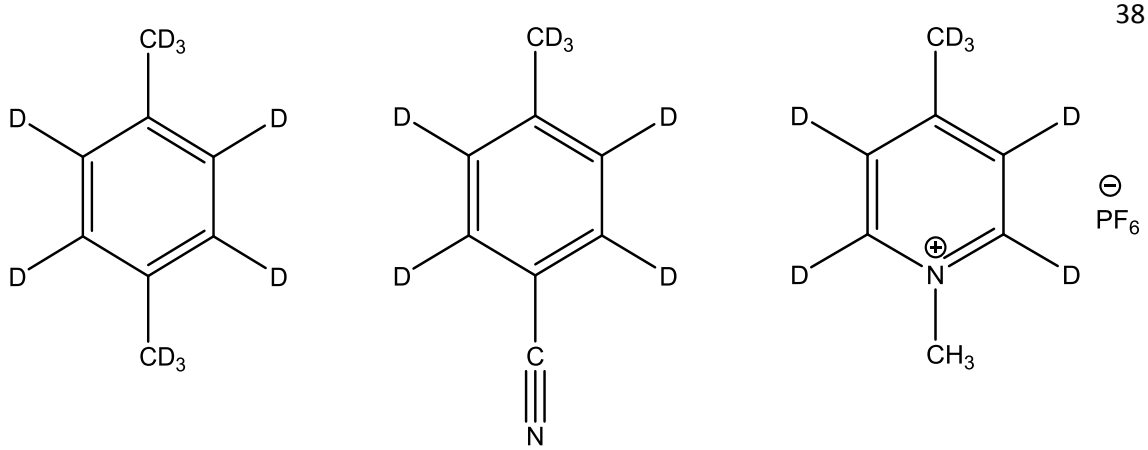

Figure 6.1. Rotational probes used in this work (from left to right) were p-xylene-d_{10} (pXy^0), p-tolunitrile-d_7 ($CMBz^H$), and 1,4-dimethylpyridinium-d_7 hexafluorophosphate ($DMPy^+$).

6.4. Results and Discussion

6.4.1. NMR Measurements

Measurements taken for all of the probes in $[Im_{41}][BF_4]$ resulted in good signal-to-noise ratios for temperatures greater than or equal to -15°C (Figure 6.2). Below this temperature, the broadening of the signal became excessive and was not possible to conclude anything from it. To calculate the T_1 value from the software, the peak of interest was selected, and the intensity of the peak was plotted as a function of the delay time and fit to an exponential decay.

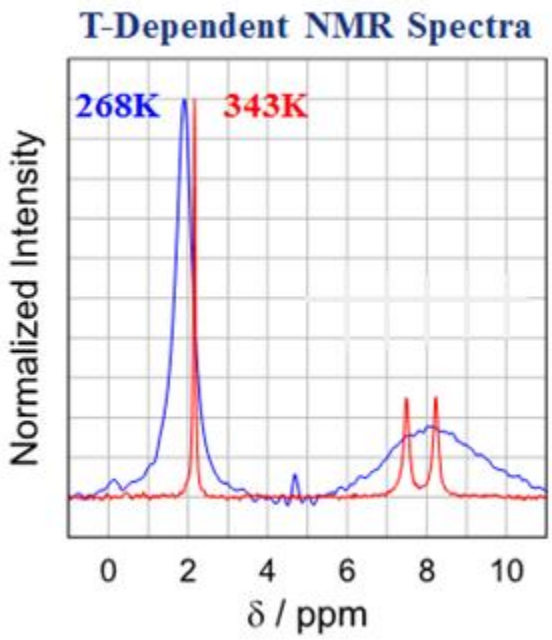

Figure 6.2. NMR spectra of $DMPy^+$ at high and low temperatures. When the temperature is high, the S/N is high, and peaks are resolvable. As the temperature decreases, the signals become broad, however S/N is still reasonable enough to obtain a relaxation time. When the temperature becomes too low, the peak broadening becomes too dominant and poor S/N is obtained.

When the temperature series of each probe is plotted (Figures 6.3 and 6.4), the T_1 minima and the dependence on the Larmor frequency is evident at low temperatures, which is expected. For the ring deuterons of the same probe, the Larmor frequency dependence falls off at higher temperatures, resulting in T_1 values measured on the 850 and 300 to converge. Additionally, pyridinium and p-xylene appear to possess similar T_1 values, while the p-tolunitrile data is well separated. Because of the independence from the Larmor frequency at higher temperatures studied, it appear that the extreme narrowing limit has been achieved for T>300K in all three solutes. With respect to the CD_3 deuterons within the same probe, the T_1 data determined on the 850 does not overlap with the 300 T_1 data, suggesting that the motion narrowing limit has not been reached. However, at a single Larmor frequency, the pyridinium and p-xylene T_1 values are still in reasonable agreement with one another at higher temperatures, while p-tolunitrile still remains well separated. The reason for this behavior is presently unknown. One thing that must be considered about the $–CD_3$ deuterons is that there are two rotations that are occurring. Along with the rotation associated with the tumbling of the molecule, there is relatively free rotation about the $–CD_3$ bond. Unfortunately, the T_1 data does not discern between the two rotations and therefore deconvolution is required, which will be detailed in the upcoming sections.

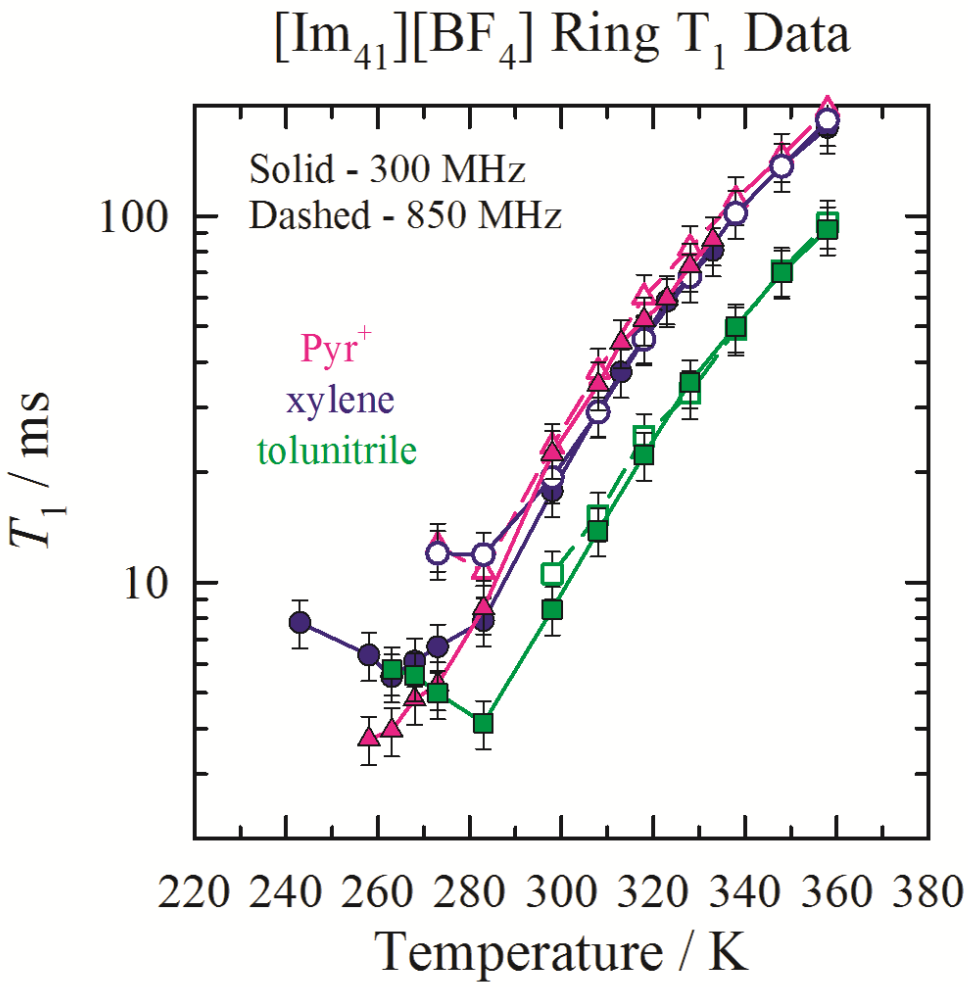

Figure 6.3. T_1 as a function of temperature for the ring deuterons of pXy^0 (blue circles), $CMBz^{\mu}$ (green squares), and $DMPy^+$ (pink triangles) in $[Im_{41}][BF_4]$. The solid symbols and lines denote data recorded on the 300MHz spectrometer and the open symbols and dashed lines the 850MHz spectrometer.

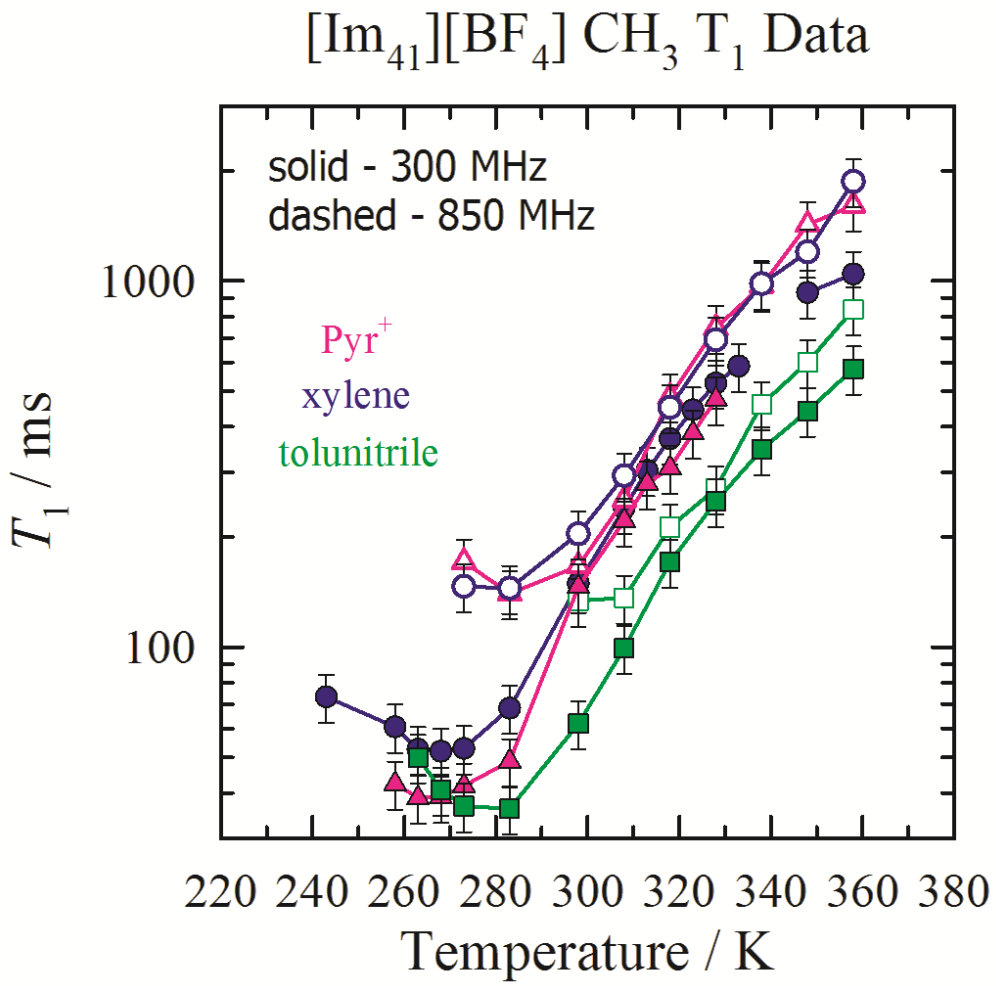

Figure 6.4. T_1 as a function of temperature for the methyl deuterons of pXy^0 (blue circles), $CMBz^{\mu}$ (green squares), and $DMPy^+$ (pink triangles) in $[Im_{41}][BF_4]$. The solid symbols and lines denote data recorded on the 300MHz spectrometer and the open symbols and dashed lines the 850MHz spectrometer. Within the same field strength, the value of T_1 for $DMPy^+$ and pXy^0 are still fairly close while $CMBz^{\mu}$ remains separate. However, the 300 MHz and 850 MHz measurements of the same probe do not converge, implying that the motional narrowing limit is not obtained.

6.4.2. MD Simulations

The T_1 data alone does not reveal any information about the functional form of the rotational relaxations of the molecules, whereas molecular dynamics (MD) simulations reveal the complete rotational correlation function. Simulations using the model "ILM2", a generic ionic liquid having properties close to those of $[Im_{41}][PF_6]$, were performed by Chris Rumble of the Maroncelli group. This model was also used in previous studies on benzene rotational dynamics.

The NMR experiments report on rotational motion of the C-D bond vectors. In the experimental probes, both C-D vectors in the aromatic plane as well as those in the CD_3 groups were measured. Simulated rotational correlation functions were therefore calculated along the ring C-D and the C-CD_3 directions as shown in Figure 6.5. Because two vectors have been assigned to the probes, two correlation functions will be calculated, the pink vector representing the "proton axis" correlation function and the red representing the "methyl axis" correlation function. The simulations were run for a 150-200 ns with 5 fs steps at temperatures of 300 K, 325 K, 375 K, and 400 K. The rotational correlation functions were calculated from 0-4 ns in steps of 0.4 ps, resulting in 10,000 total points (Figure 6.6 – 6.8).

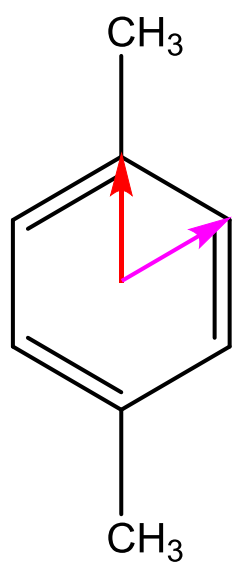

Figure 6.5. Vector assignments used in the MD simulations for pXy^0. The red vector represents the methyl vector and the pink represents the proton vector.

6.4.3. Fitting the Rotational tcfs

6.4.3.1. Proton Axis Rotational tcf Fitting

With the rotational correlation functions calculated for the vectors of each probe, the next step in the analysis is to find a functional form that best fits the simulated functions. The fitting was done by using a least squares minimization in MATLAB, sampling a range of various equation types. Some equations that were tested include single and sums of two and three exponentials, lognormal + exponential, lognormal + stretched exponential, and exponential + stretched exponential. The optimal fit was selected on the basis of providing a quality fit and possessing a relatively simple form. Of the equations tested, the exponential + stretched exponential function was chosen.

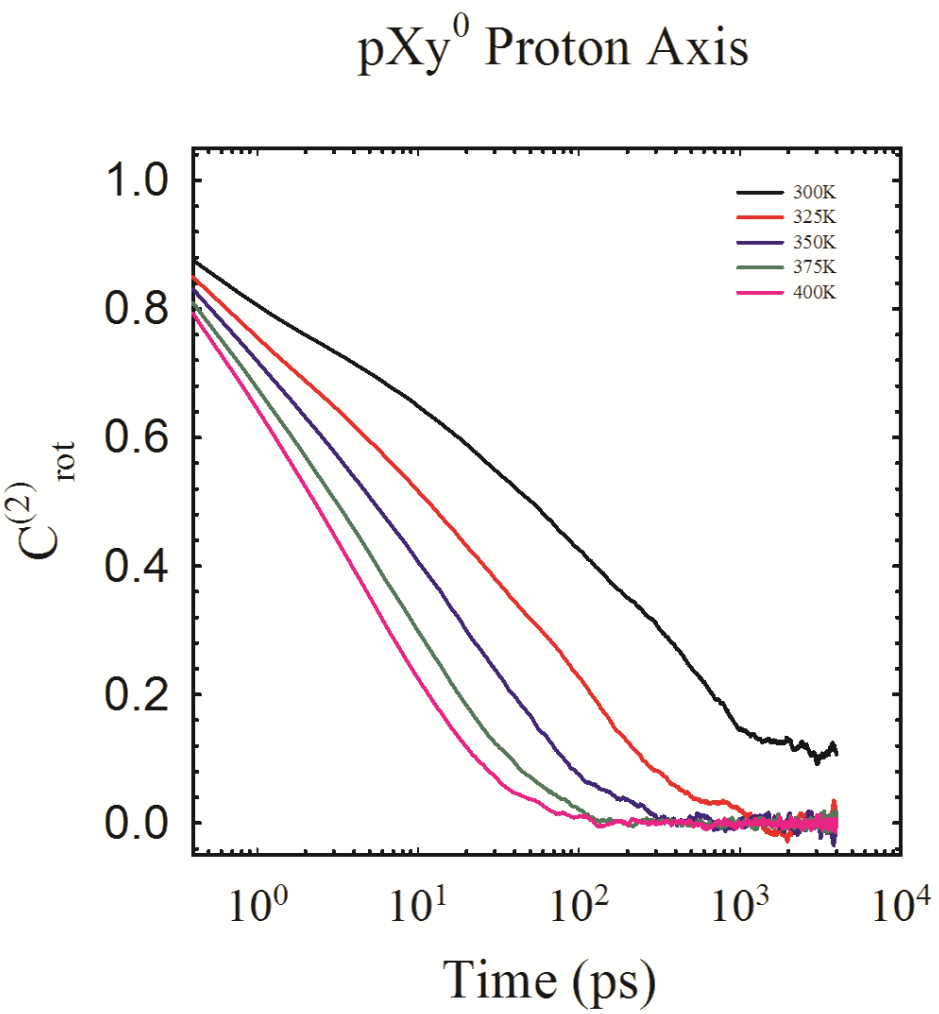

Figure 6.6. Temperature dependent time correlation functions of the proton axis in pXy^0 calculated from MD simulations.

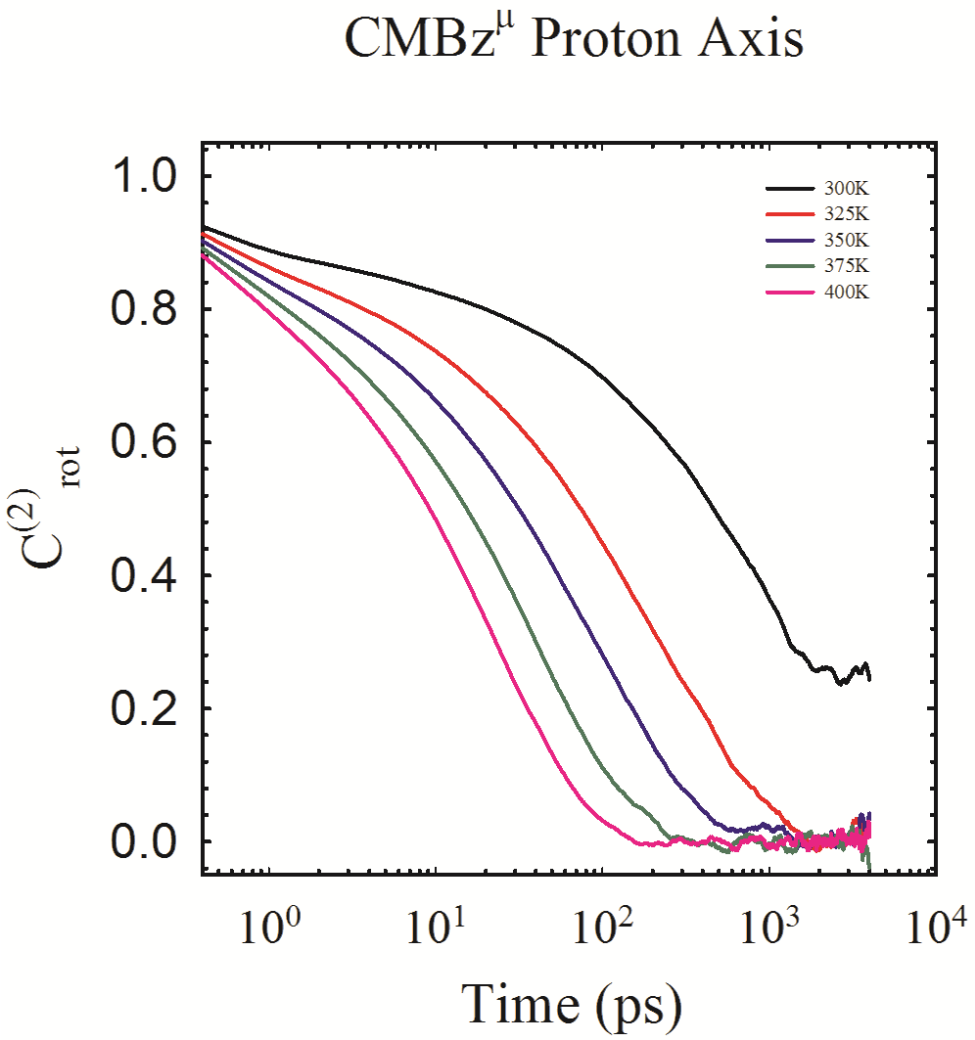

Figure 6.7. Temperature dependent rotational tcfs of the proton axis in CMBz$^{\mu}$ calculated from MD simulations.

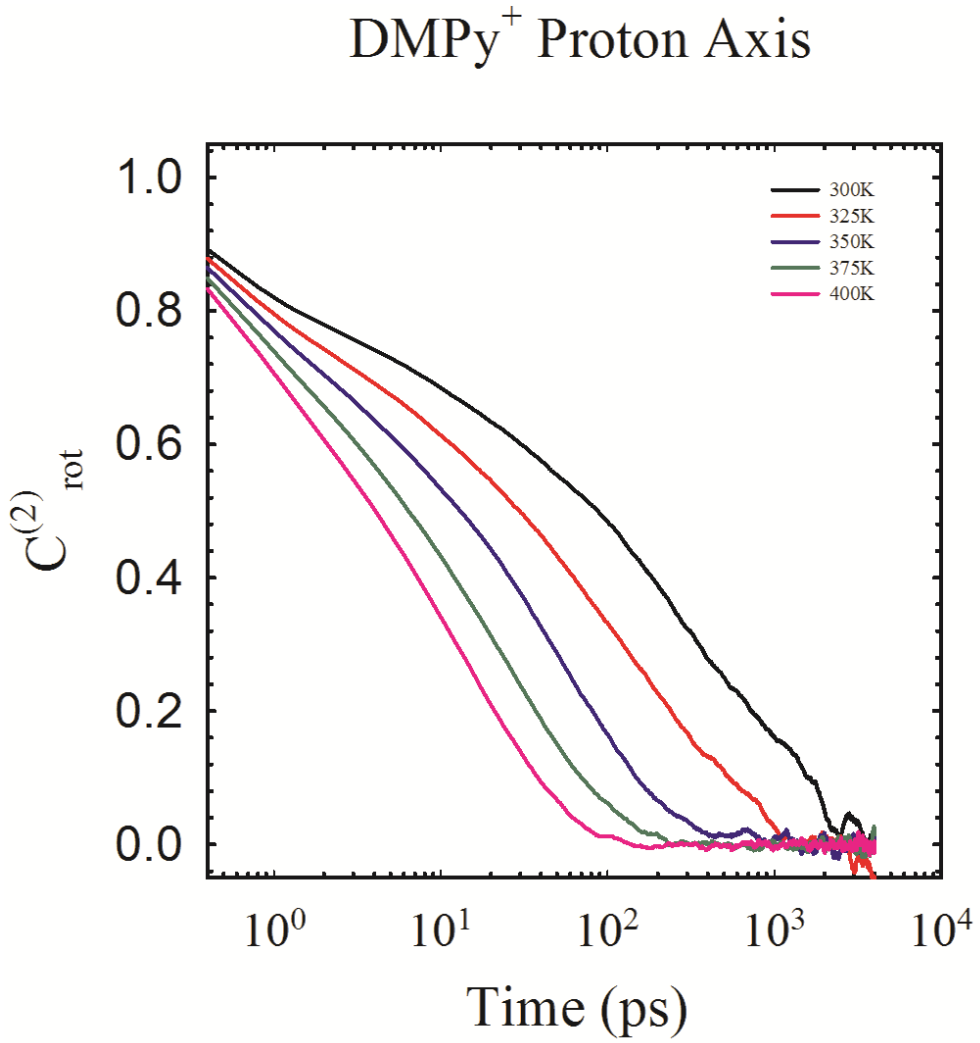

Figure 6.8. Temperature dependent rotational tcfs of the proton axis in $DMPy^+$ calculated from MD simulations.

The exponential + stretched exponential function for the proton axis rotational tcf has the following format:

$$C_{rot}^{(2)}(t) = Ae^{-t/\tau_1} + (1-A)e^{-(t/\tau_2)^{\beta}} \qquad 6.3$$

where A is the fraction of the function represented by the exponential fit, τ_1 is the time constant of the exponential component, τ_2 is the time constant of the stretched exponential component, and β is the stretching parameter. The best fit parameters of each probe are provided in Tables 6.1-6.3.

Table 6.1: pXy^0

T / K	**A**	**τ_1**	**1-A**	**τ_2**	**β**
300	0.102	0.778	0.898	234.4	0.358
325	0.142	0.75	0.858	47.8	0.449
350	0.154	0.756	0.846	18.8	0.516
375	0.168	0.738	0.832	9.8	0.573
400	0.175	0.798	0.825	6.7	0.594

Table 6.2: CMBz$^{\mu}$

T / K	**A**	**τ_1**	**1-A**	**τ_2**	**β**
300	0.097	0.422	0.903	1448.1	0.491
325	0.107	0.483	0.893	186.7	0.57
350	0.113	0.504	0.887	77.3	0.607
375	0.126	0.528	0.874	35.4	0.676
400	0.146	0.541	0.854	21.3	0.748

Table 6.3: DMPy$^+$

T / K	A	τ_1	1-A	τ_2	β
300	0.153	0.637	0.847	321.7	0.459
325	0.163	0.657	0.837	112.3	0.497
350	0.18	0.637	0.82	44.3	0.577
375	0.184	0.652	0.816	21.1	0.616
400	0.217	0.648	0.783	13.2	0.686

Tables 6.1 – 6.3. Parameter values from the correlation function of the proton axis from each probe.

Tables 6.1-6.3 indicate that there is a temperature dependence of the fitting parameters, which is particularly strong in the case of τ_2. Temperature dependence of the correlation times can be fit based upon the models

$$\tau_1(T) = \tau_1^{ref}\left(\frac{T_{ref}}{T}\right)\left(\frac{\eta}{\eta_{ref}}\right)^p \qquad 6.4$$

$$\tau_2(T) = \tau_2^{ref}\left(\frac{T_{ref}}{T}\right)\left(\frac{\eta}{\eta_{ref}}\right)^p \qquad 6.5$$

where T_{ref} is a reference temperature, η_{ref} is the viscosity of the solvent at the reference temperature , τ_1^{ref} is the correlation time of the exponential at the reference temperature, τ_2^{ref} is the correlation time of the stretched exponential, and p is a measure of how influential the viscosity is on the correlation time. In addition to the correlation time parameters expressing temperature dependence, the stretching parameter, β, also contains this dependence. Unlike correlation times, the temperature-viscosity model for β does not follow a power law relationship, but rather a linear one. Temperature and viscosity dependence of the correlation times and the temperature dependence of β is incorporated into the overall correlation function $C_{rot}^{(2)}(t)$ to give a function that is dependent on time and temperature.

$$C_{rot}^{(2)}(t,T) = Ae^{-t/\tau_1(T)} + (1-A)e^{-(t/\tau_2(T))^{\beta(T)}} \qquad 6.6$$

6.4.3.2. Proton Axis NMR Fitting

By knowing the basic functional form of the temperature dependent rotational correlation functions, the next step in the analysis is to fit the NMR data. The parameters in the temperature dependent rotational tcf (A, τ_1^{ref}, τ_2^{ref}, p, and β) were fixed or varied systemically to generate a set of T_1 values at the same temperatures used in the experiments based upon Eq. 2.5 and Eq. 2.6. Figures 6.9-6.11 depict the theoretical (lines) and experimental (circles, triangles) T_1 sets as a function of temperature. It is evident for each probe from the agreement between the two plots that the relaxation times were successfully recreated, and a rotational correlation function was extracted. Comparing the simulated rotational tcfs to the NMR derived rotational tcfs for each probe resulted in similar line shapes with reasonable agreement.

From the rotational tcfs determined by the NMR fits, the average correlation times,$\langle\tau_{rot}\rangle$, were determined as a function of ηT^{-1} for each of the probes. As seen in Figure 6.12, the CMBz$^{\mu}$ $\langle\tau_{rot}\rangle$ is well separated from the other average rotational correlation times of the other probes. This trend is consistent with the T_1 behavior that is observed in Figure 6.3 where the relaxation times are much lower, which is congruent with a larger rotation time. The $\langle\tau_{rot}\rangle$ of pXy^0 and DMPy$^+$ are also consistent with the temperature dependent T_1 behavior; at higher temperatures, DMPy$^+$ T_1 values are nearly identical to pXy^0, paralleled by the nearly identical $\langle\tau_{rot}\rangle$, and as the temperature decreases, T_1 of DMPy$^+$ becomes smaller than pXy^0, indicating it rotates more slowly than pXy^0. The analogous behaviors between $\langle\tau_{rot}\rangle$ determined from NMR fit rotational tcf and the temperature dependent T_1 plots substantiate the NMR fitting process with the assistance of MD simulations.

All probes selected in this study were done so on the basis of having similar size and shape constraints, leading to any deviations being caused presumably from the solute-solvent interactions. It is reasonable to assume that stronger interactions between the solute and solvent would lead to slower rotations of the probe, and from this hypothesis, the charged probe is expected to have the slowest rotation times. When the $\langle\tau_{rot}\rangle$ are compared, the observed behavior does not support this hypothesis. Rotational correlation times determined for pXy^0 and DMPy$^+$ are comparable, with DMPy$^+$ rotating faster until high temperatures are reached and both are rotating just as fast. While this behavior is consistent with the NMR measurements, it is

evident that the average rotational correlation times for these probes are not solely governed by the solute-solvent interactions. While size and shape are presumably consistent within the series, they are not identical. Hydrodynamics is very sensitive to size and shape concerns and further analysis will be required based upon these variables in order to precisely describe the observations reported in this study. One possible explanation for the behavior draws upon the difference between the nitrile and methyl functional groups. The pXy^0 and $DMPy^+$ possess the most closely related size and shape conditions due identical functional groups on the ring, but the nitrile on $CMBz^\mu$ is larger than a methyl group. It is possible that the larger size of the functional group would result in a larger rotational correlation time, while the identical functional groups possess comparable values.

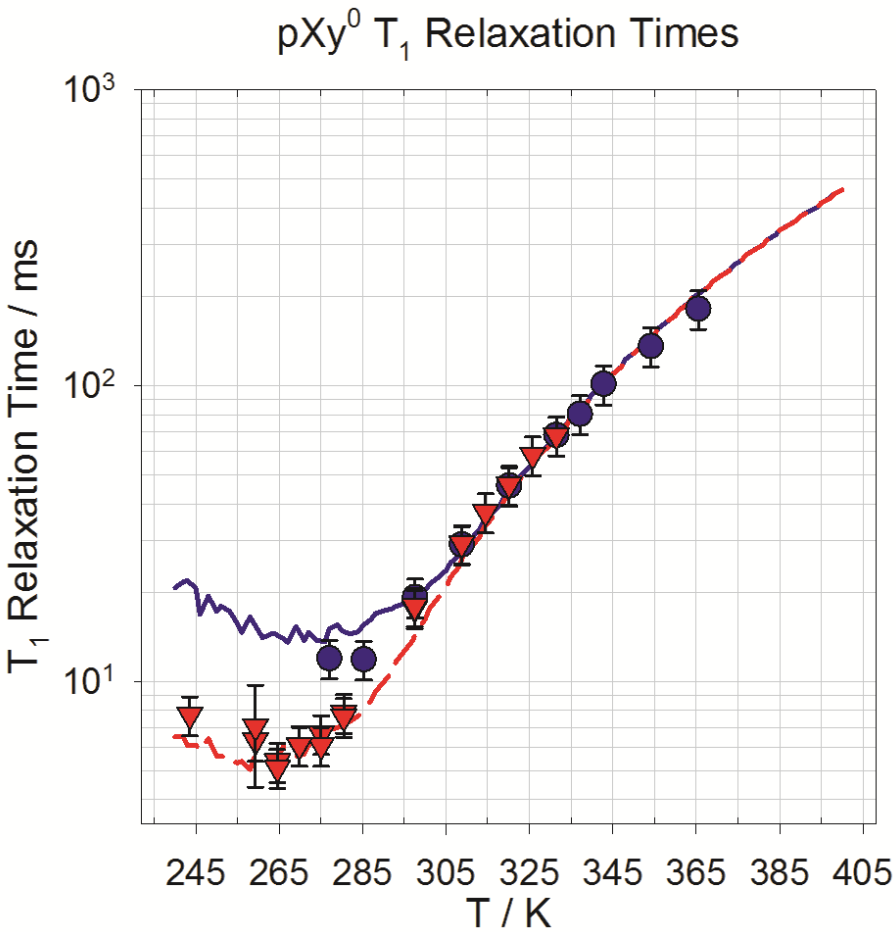

Figure 6.9. Experimental data (blue circles for 850 MHz and red triangles for 300 MHz) are fit by different combinations of parameters (blue and red lines).

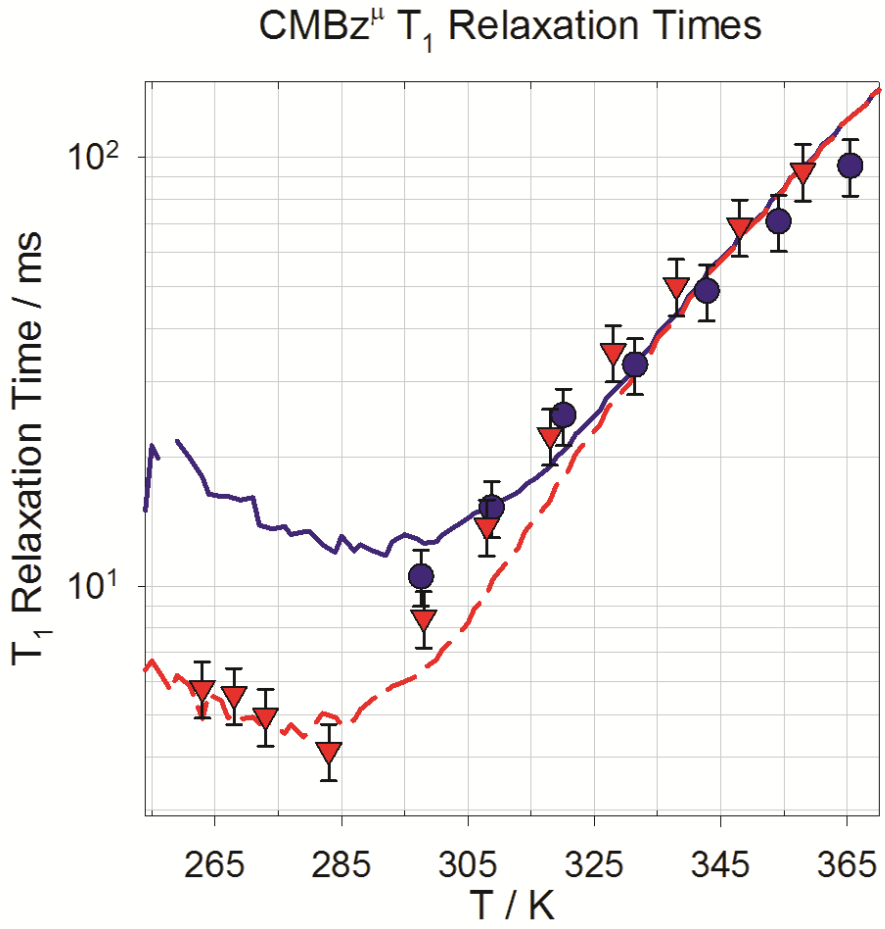

Figure 6.10. Experimental data (blue circles for 850 MHz and red triangles for 300 MHz) are fit by different combinations of parameters (blue and red lines).

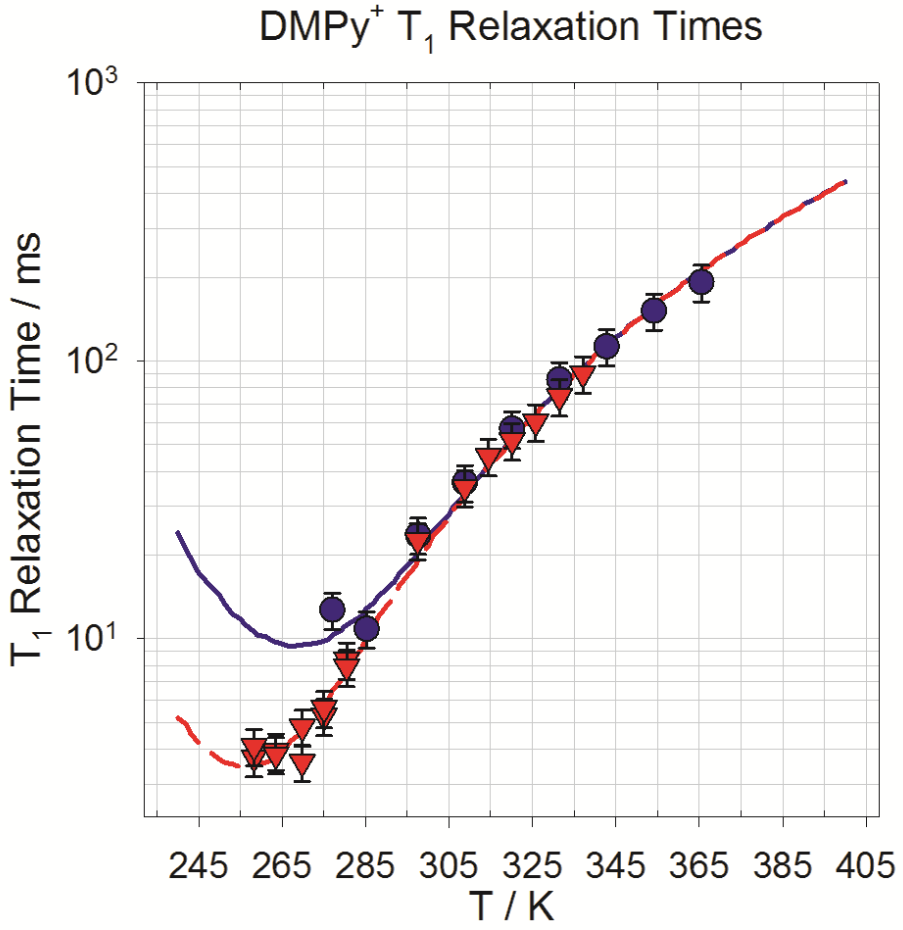

Figure 6.11. Experimental data (blue circles for 850 MHz and red triangles for 300 MHz) are fit by different combinations of parameters (blue and red lines).

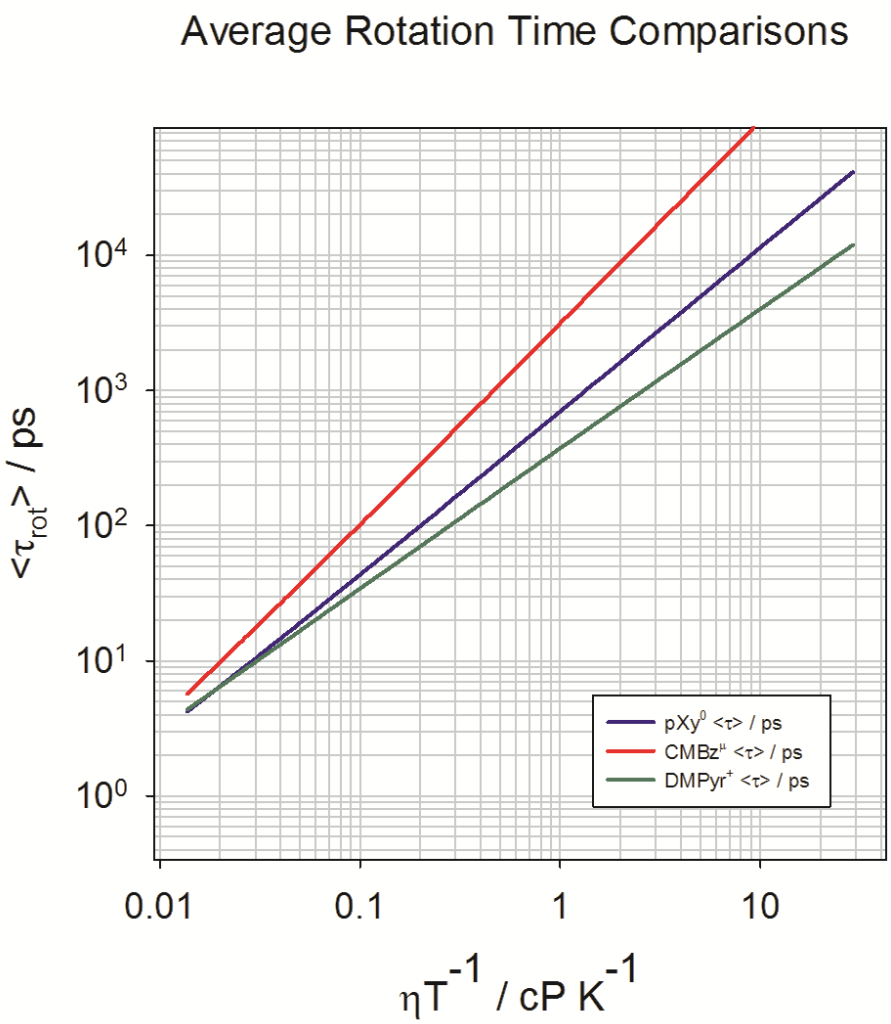

Figure 6.12. Rotational correlation times extracted from fits of the NMR data.

6.4.3.3. Methyl Axis Fitting

In a comparable way, the functional form of the rotational tcfs of the methyl axis vectors calculated from MD simulations was determined through a least squares minimization in MATLAB and the parameter values from simulation were recorded (Tables 6.4 – 6.6). Unlike the proton axis, the methyl C-D bonds have two rotations that will relax the correlation function; one from the molecular tumbling and the other from free rotation about the $–CD_3$ bond. In the simulations, the designated vector only accounts for the molecular tumbling of the molecule. The rotational tcf needs to incorporate a factor that will account for this additional rotation when performing the NMR fits since this rotation is part of the T_1 data. Lipari *et. al.* state that if an internal rotation ($C_I(t)$), such a methyl rotation, and the correlation function of the overall system ($C_O(t)$) are independent, the rotational correlation function can be described by

$$C_{rot}^{(2)} = C_I(t)C_O(t) \qquad 6.7$$

where $C_O(t)$ is the exponential + stretched exponential correlation function and $C_I(t)$ is

$$C_I(\mathrm{t}) \approx S^2 + (1 - S^2)e^{-t/\tau_e} \qquad 6.8$$

where S is a "general order parameter" that describes the spatial restriction of the methyl rotation and τ_e is its correlation.[10] The value of S is determined by

$$S = P_2(\cos\beta) \qquad 6.9$$

where $P_2(x)$ is the second rank Legendre polynomial and β is angle between the C-D bond and the symmetry axis of the $–CD_3$ bond, which for a perfect tetrahedron is 70.5°. Scaling τ_e with temperature and viscosity in the same fashion as $\tau_1$and τ_2 and substituting Eq.6.6 and Eq. 6.8 into Eq. 6.7, the functional form of the rotational tcf for the methyl deuterons is obtained.

$$C_{rot}^{(2)}(t,T) = (Ae^{-t/\tau_1(T)} + (1 - A)e^{-(t/\tau_2(T))^{\beta(T)}})(S^2 + (1 - S^2)e^{-t/\tau_e(T)} \qquad 6.10$$

Table 6.4: pXy^0

T / K	A	τ_1	1-A	τ_2	β
300	0.079	1.06	0.921	581.7	0.375
325	0.112	0.926	0.888	96.1	0.483
350	0.141	0.934	0.859	37.2	0.569
375	0.159	0.996	0.841	19.5	0.615
400	0.184	0.941	0.816	13.1	0.677

Table 6.5: CMBz$^{\mu}$

T / K	A	τ_1	1-A	τ_2	β
300	0.077	0.449	0.923	2967.1	0.501
325	0.094	0.512	0.906	301.5	0.637
350	0.095	0.534	0.905	120.5	0.641
375	0.109	0.57	0.891	52.6	0.716
400	0.123	0.589	0.877	30.9	0.78

Table 6.6: DMPy$^+$

T / K	A	τ_1	1-A	τ_2	β
300	0.076	0.656	0.924	2646.9	0.402
325	0.1	0.645	0.9	338.4	0.53
350	0.113	0.67	0.887	109.8	0.616
375	0.121	0.7	0.879	52.0	0.658
400	0.135	0.717	0.865	28.0	0.715

Tables 6.4 – 6.6. Parameter values from the correlation function of the methyl axis from each probe.

For the NMR fits, A, τ_1^{ref}, τ_2^{ref}, p, β, τ_e^{ref}, and S were set or varied by steps in a parallel manner to the proton axis fitting. The experimental T_1 values were fit based upon the parameter values that resulted in the closest recreation of the data, which can be seen in Figures 6.13-6.15. Once again, recreation of the T_1 values determined from experiment was successful and the rotational tcfs of the methyl C-D bond were obtained, which are also in agreement with the tcfs calculated by simulation (Figures 6.16-6.18). It is evident from the successful recreation of the

T_1 data that incorporation of the methyl rotation is possible, and will not limit the analysis to static C-D bonds.

Figure 6.19 displays the rotational correlation times for each probe as a function of ηT^{-1}. As is the case for the proton rotation times, the CMBz$^{\mu}$ $\langle \tau_{rot} \rangle$ are well separated from the other two probes, possessing a larger average correlation time, which is comparable to the T_1 data where the values are much lower. The pXy^0 and DMPy$^+$ $\langle \tau_{rot} \rangle$ are nearly identical over the entire range of T^{-1} , which is also alike to the T_1 values being similar over the range of temperatures that they were measured. This observation further supports claims that the solute-solvent interactions are not as influential on the rotational dynamics based on comparable explanations from the proton data.

Although the $\langle \tau_{rot} \rangle$ and T_1 values are in agreement for all probes, it is evident that the motional narrowing limit has not been reached. While this does not affect the processing of the data, it is curious result that is not quite understood. Given the frequencies of the instruments that the measurements were performed on, the motional narrowing limit should be obtained when rotational correlation times are significantly less than a few nanoseconds, a condition that is met according to the correlation functions derived from the NMR fits. As a result, it would seem that the difference could be attributed to poor experimental measurements, however it seems unlikely given the proton data is significantly less skewed between instruments. Alternatively, such behavior could be intrinsic to methyl group rotation. In order to truly test either of these options, additional measurements will be needed for both pXy^0 and DMPy$^+$, and possibly using another probe that is similar to the ones already used, such as toluene.

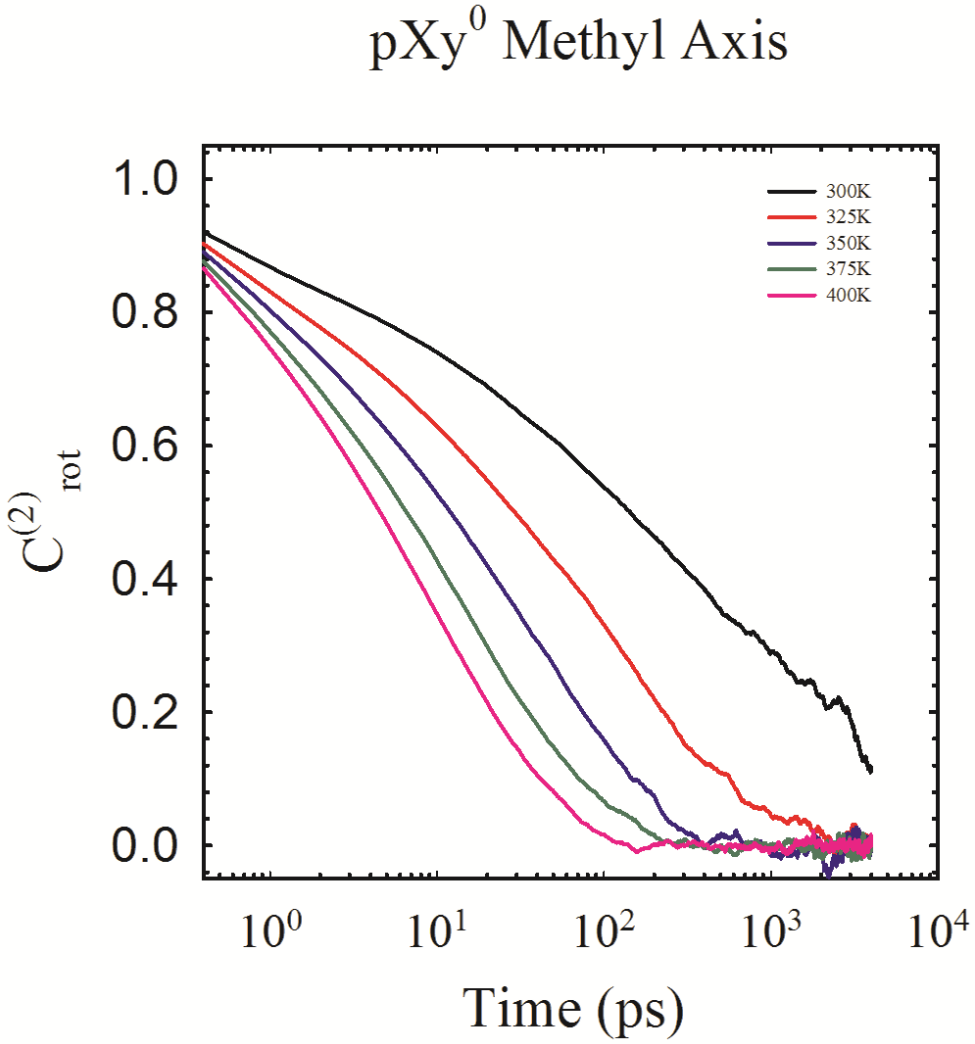

Figure 6.13. Rotational tcfs of the methyl axis of pXy^0 still fit to the exponential + stretched exponential despite the additional rotation. The free rotation was not calculated from MD simulations.

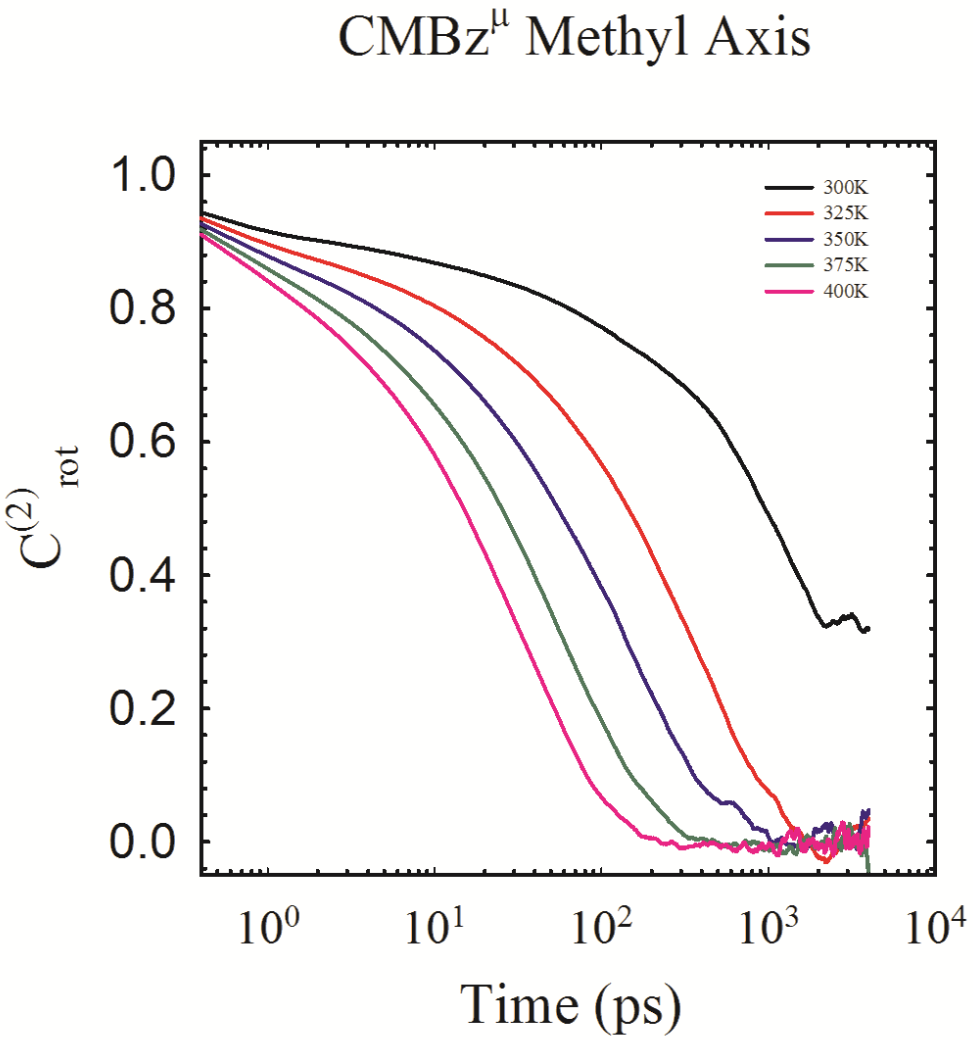

Figure 6.14. Rotational tcfs of the methyl axis of CMBz$^{\mu}$ still fit to the exponential + stretched exponential despite the additional rotation. The free rotation was not calculated from MD simulations.

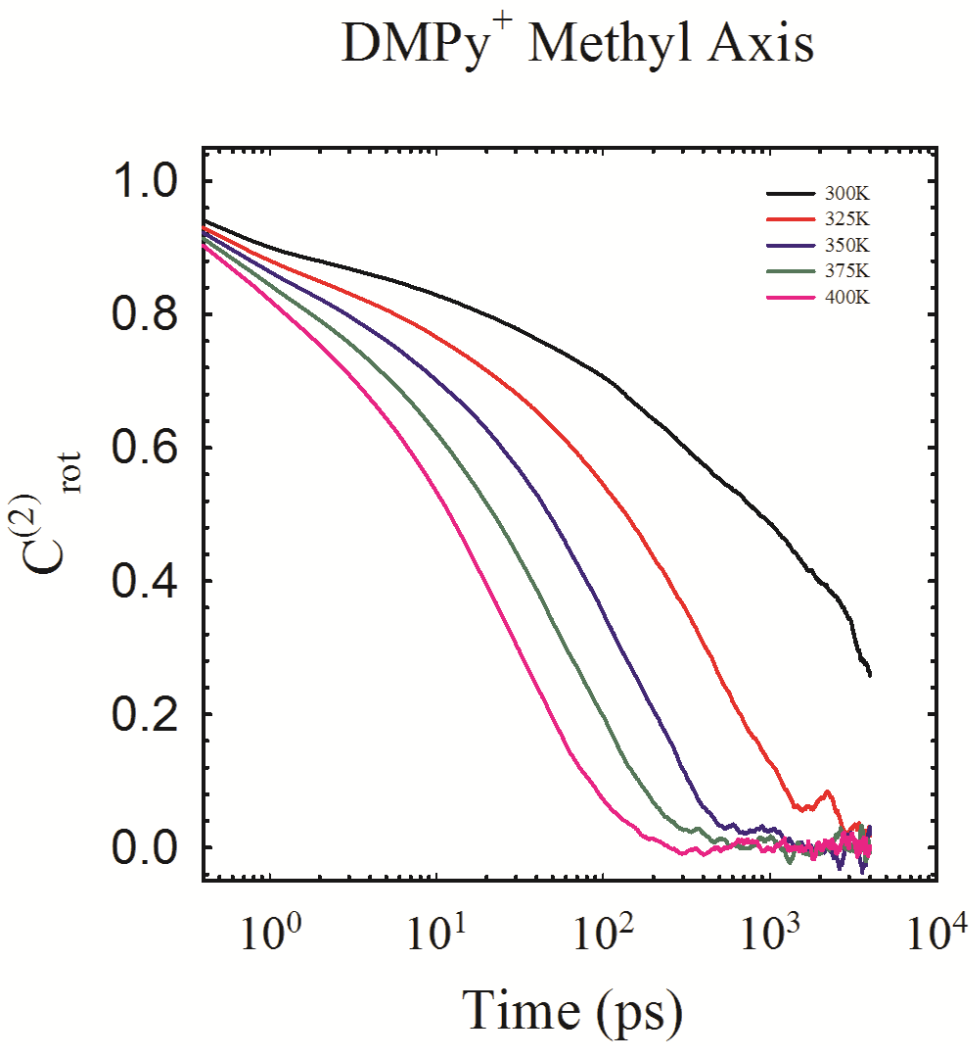

Figure 6.15. Rotational tcfs of the methyl axis of $DMPy^+$ still fit to the exponential + stretched exponential despite the additional rotation. The free rotation was not calculated from MD simulations.

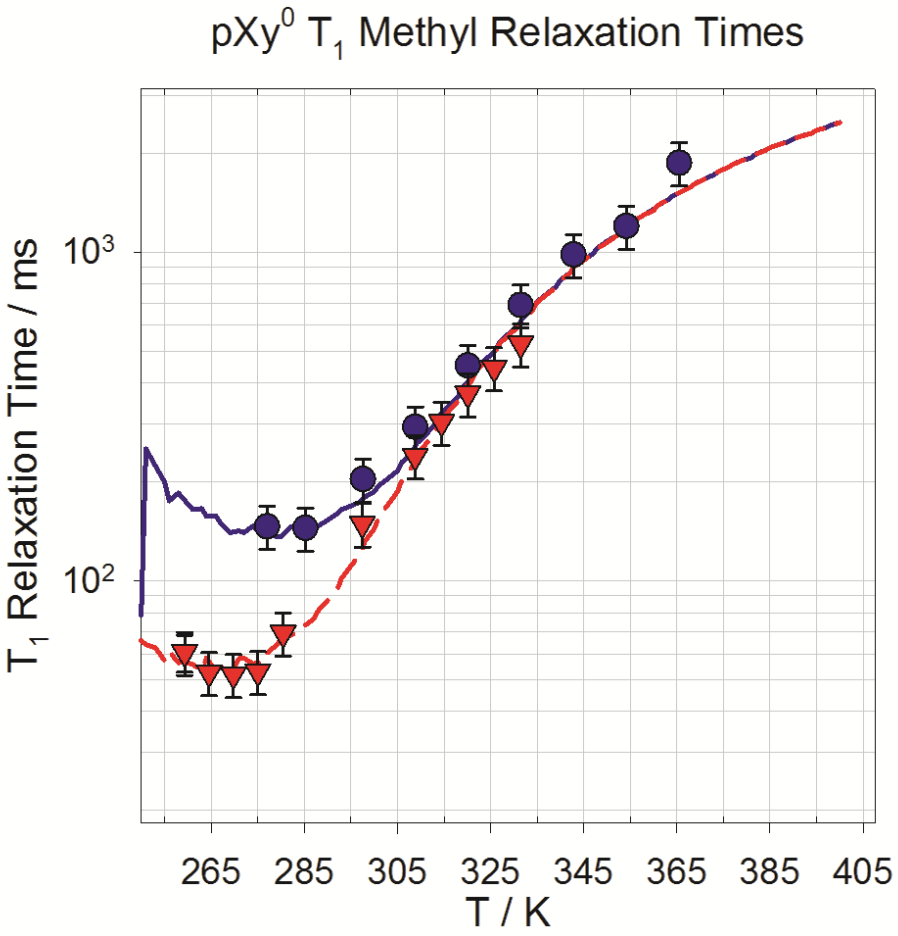

Figure 6.16. Experimental data (blue circles for 850 MHz and red triangles for 300 MHz) are fit by different combinations of parameters (blue and red lines).

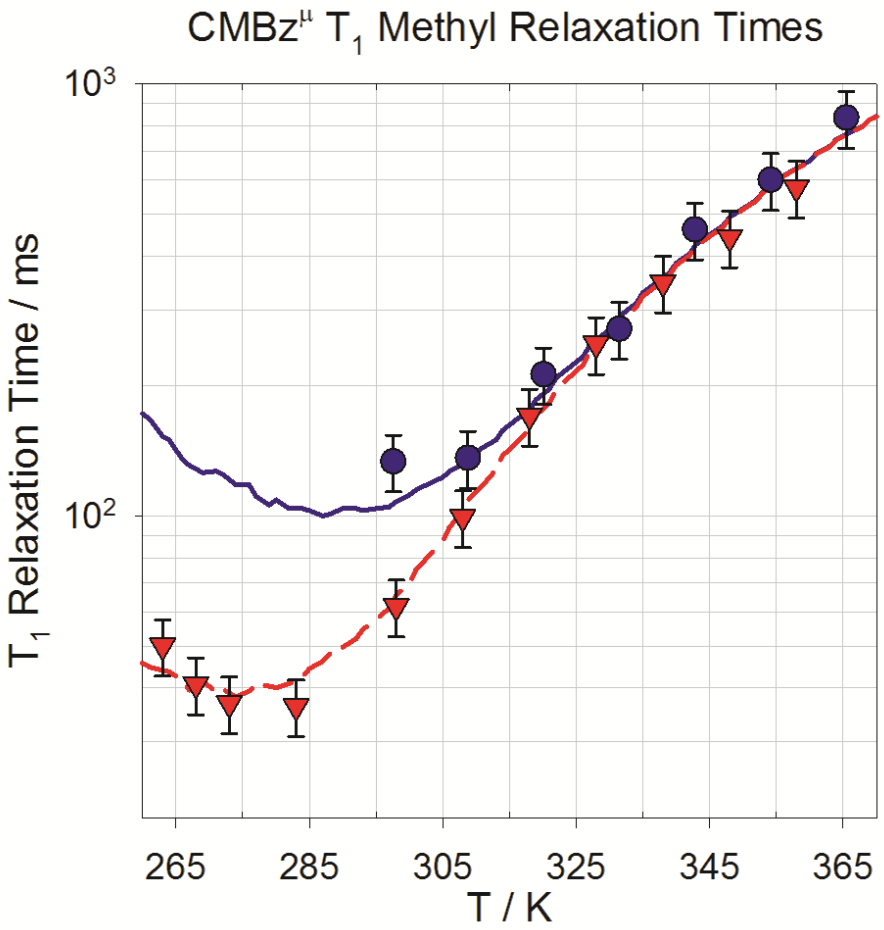

Figure 6.17. Experimental data (blue circles for 850 MHz and red triangles for 300 MHz) are fit by different combinations of parameters (blue and red lines).

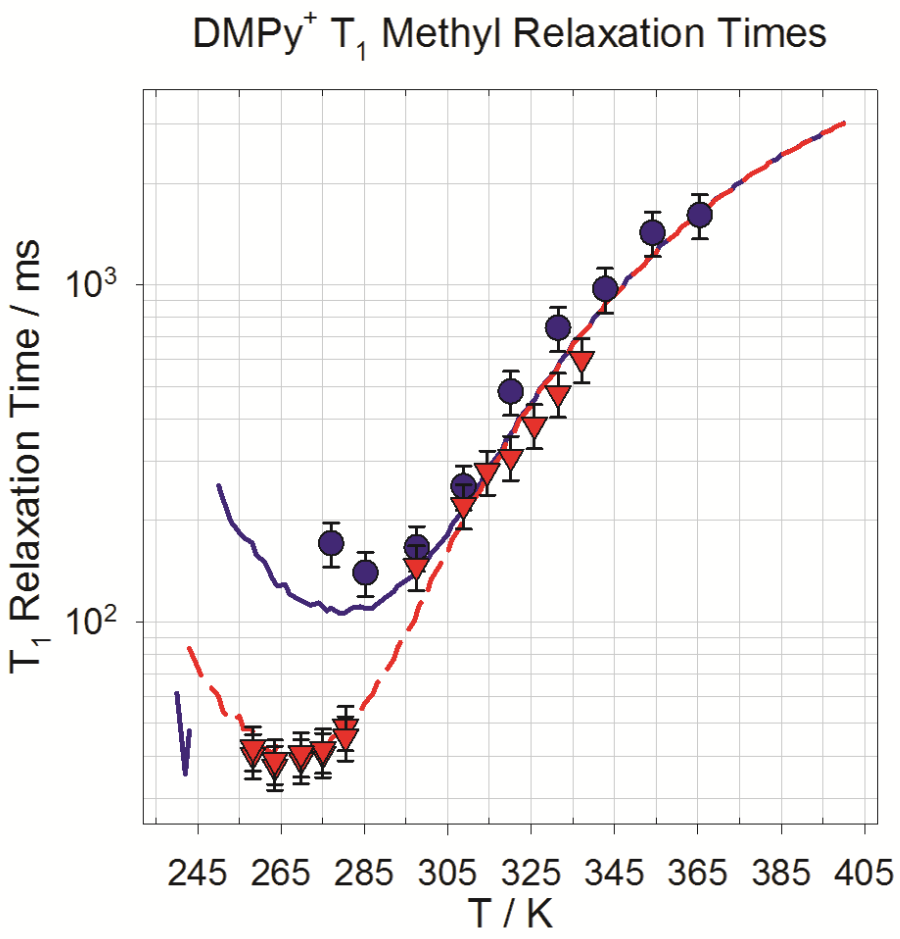

Figure 6.18. Experimental data (blue circles for 850 MHz and red triangles for 300 MHz) are fit by different combinations of parameters (blue and red lines).

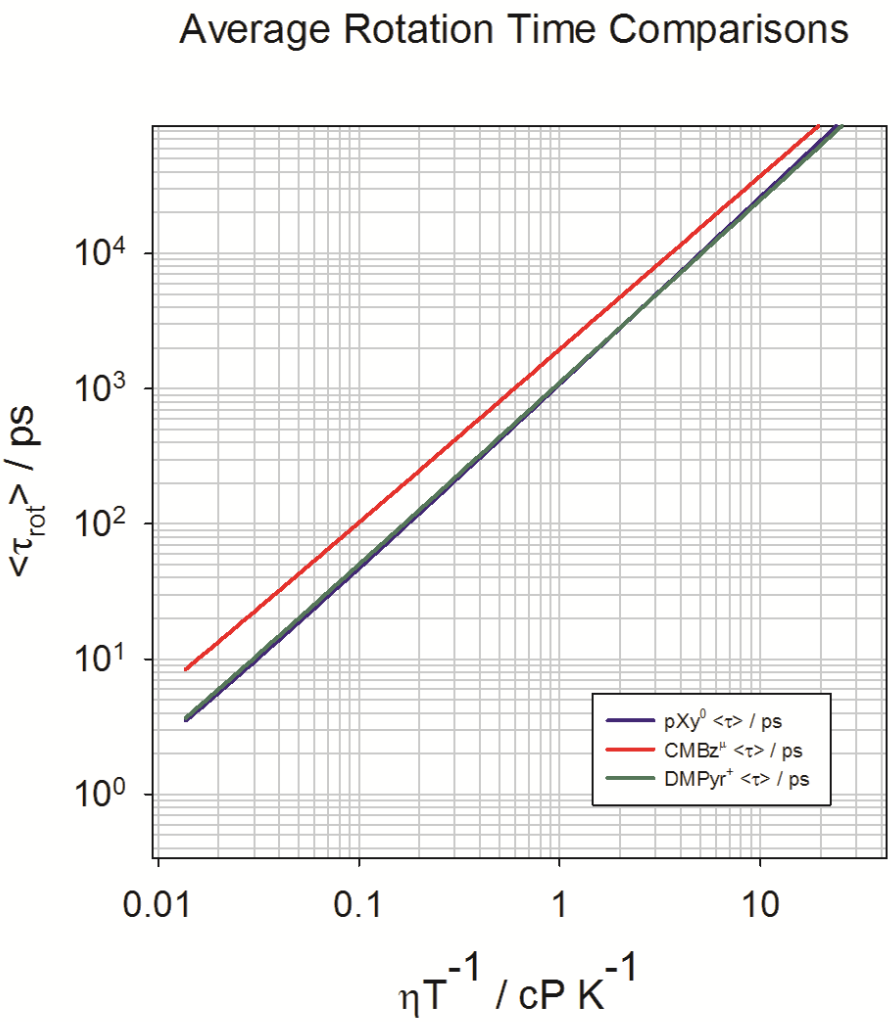

Figure 6.19. Rotational correlation times extracted from fitting the methyl proton data.

6.4.4. Summary and Conclusions

The goal of this study was to observe the effects that solute-solvent interactions would have on the rotational dynamics of probes with similar size and shape in $[Im_{41}][BF_4]$. It was hypothesized that stronger interactions between the solute and solvent would cause rotation of the probes to be slower, meaning a larger average rotational correlation time. To test this, deuterium inversion recovery experiments were performed over a temperature range on two different instruments to obtain longitudinal relaxation times. By fitting the relaxation times based upon a functional form of an exponential + stretched exponential derived from MD simulations, the average rotational correlation times of the C-D bond on the ring and methyl groups of each probe could be determined.

In the case of the proton axis, there was strong agreement between the experimental NMR data and the recreated T_1 values from the fitting program, yielding a similarly shaped rotational tcf to those derived from MD simulations. The successful recreation of the experimental NMR data supports extraction of a rotational tcf in this manner. The ordering of rotation times observed was not what was expected, specifically for pXy^0 and $DMPy^+$. Despite the two probes possessing different interactions with the solvent, the rotational correlation times were very similar, with $DMPy^+$ actually rotating faster at higher temperatures. For both, the average rotational correlation times were smaller than that of $CMBz^{\mu}$, which could be attributed to the larger nitrile functional group attached to the ring. With respect to size and shape, pXy^0 and $DMPy^+$ are most closely related, which may account for the congruent rotational behavior, suggesting that for molecules of this size, charge does not seem to have an effect on rotation.

Another challenge of this study was analyzing rotation of a C-D bond within a methyl group. In previous studies, the deuterium bonds considered were only influenced by the overall tumbling of the molecule. In the case of the methyl deuterium bond, molecular tumbling and the free rotation of the functional group are both capable of relaxing the correlation function and therefore required more complicated analysis. By making the assumption that the total rotational tcf is the product of two independent rotational correlation function, one for molecular tumbling and the other for the methyl rotation, a modified functional form of the rotational tcf was used in fitting the NMR data. Despite the unfamiliar processing, T_1 values were recreated that agreed

reasonably with the experimental data. Like the proton observations, the $\langle\tau_{rot}\rangle$ and T_1 values are consistent for all probes and the CMBz$^{\mu}$ $\langle\tau_{rot}\rangle$ was well separated from the others. In contrast, the pXy^0 and DMPy$^+$ average rotational correlation times were nearly identical over the entire ηT^{-1} range. Though the methyl and proton data do not have identical relationships between the $\langle\tau_{rot}\rangle$ of pXy^0 and DMPy$^+$, both sets of data further support the idea that solute-solvent interactions do not seem to govern the rotational diffusion of the molecules.

One discrepancy with the methyl data is that from the T_1 plots, it would appear that the motional narrowing limit has not been reached. Within the same instrument, the relaxation times of pXy^0 and DMPy$^+$ seem to overlap, however the values determined on the 300 MHz instrument do not match with the values obtained for the 850 MHz instrument at high temperatures. Based upon the frequencies the instruments, the rotational correlation times should be less than 2-3 ns to reach the motional narrowing limit, which is far more than the average correlation times calculated at high temperatures. The reasons for this discrepancy are still being explored. One explanation could be erroneous NMR data of the methyl deuterons, however this conclusion could be disputed by the quality of the proton data since it was taken from the same spectra. It is possible that the behavior observed results from an intrinsic dependence on field strength to longitudinal relaxation of methyl groups deuterons. Further experiments are required, such as repeat measurements of the probes used in this work or additional probes with methyl groups, to determine if such claims are true.

Chapter 7. Summary and Conclusions

In this study, translational and rotational diffusion in neat ionic liquids and dilute ionic liquid solutions were investigated using NMR spectroscopy. The first translational diffusion study focuses on solutions prepared in 1-alkyl-1-methylpyrrolidinium bis(trifluoromethylsulfonyl)imde ionic liquids ([Pr_{n1}][Tf_2N], *n*=3,4, and10) with quasi-spherical solutes, such as methane, ammonium, and tetramethylsilane. The second study entails measurement of self-diffusion coefficients in homologous series of neat ionic liquids: 1-alkyl-3-methylimidazolium bis(trifluoromethanesulfonyl)imide, [$C_nC_1$im][Tf_2N] and [(n-2)m$C_{n-1}C_1$im][Tf_2N] n = 3, 4, 5, 6, 7. The majority of the measurements of translational diffusion were carried out using a Bruker AV-III-850 NMR spectrometer with a Diff-30 probe with triple axis gradients using a longitudinal-eddy-current delay stimulated echo NMR pulse sequence.

The most evident deviations from the Stokes-Einstein model were present in the regime of small solute-to-solvent volume ratios, which were further distinguished by their charge. In the case of methane, the relative friction ratio indicates that diffusion is faster than SE predictions, while small, charged solutes like ammonium exhibit slower than predicted diffusion, consistent with observations from previous studies. Simulation data provided an analogous result, conveying diffusion coefficients of similar value. In addition the diffusion coefficients, simulation was able to trace the trajectory of methane and ammonium moving through the ionic liquid. Analysis of these trajectories revealed that the diffusion of methane is not governed by solute-solvent interactions, but the solvent-solvent interactions; both the polar and nonpolar domains of the ionic liquid are sampled, with high mobility being associated with low density (nonpolar domains) and slower mobility in high density (polar domains). The overall effect is enhanced diffusion, evident by the jump pattern of the trajectory. For ammonium, the retardation of diffusion is attributed to the strong attraction to the anion of the ionic liquid. Because of this attraction, the effective hydrodynamic radius of the solute is increased, therefore leading to slower, caged trajectories.

Additional translational diffusion experiments were performed on two series of neat ionic liquids which differed in either having a linear or branched alkyl chain on the cation. These liquids were provided by the Quitevis group from Texas Tech University. Diffusion coefficients of both the cations and anions of these ionic liquids were determined. The alkyl chain length

dependence of the cation diffusion coefficients for both the branched and linear ionic liquids paralleled the dependence of viscosity on chain length. In the case of the branched cations, there is an anomaly when n=4, while the linear series retains the monotonic dependence on n. In addition to the cation diffusion coefficients, anion diffusion coefficients were also determined, and they were found to express the same type of behavior observed in the cation measurements. When comparing the values of the diffusion coefficients between the cations and anions within the same liquid, the cations are diffusing faster, on average, than the anions in the case of $n \leq 6$. When $n = 7$, the diffusion coefficient for both the branched and linear cation/anion pairs appear to converge to approximately the same value. For shorter lengths, it would seem that the alkyl-chain structure has some sort of effect on the interactions between the cation/anion pairs. These observations would suggest that once the alkyl-chain length approaches a certain length, the structure of the nonpolar tail does not seem to have a distinguishing effect on the dynamics of either the cation or anion. Chemical shift data was also gathered on the cations to determine if some type of intramolecular interaction could be attributed to the anomalies observed in the branched series. While the data does show some interesting behavior, none of the results were conclusive.

The goal of the rotational diffusion study was to observe the effects that solute-solvent interactions would have on the rotational dynamics of probes with similar size and shape in $[Im_{41}][BF_4]$. It was hypothesized that stronger interactions between the solute and solvent would cause rotation of the probes to be slower, meaning a larger average rotational correlation time. To test this, deuterium inversion recovery experiments were performed over a temperature range on two different instruments to obtain longitudinal relaxation times. By fitting the relaxation times based upon a functional form of an exponential + stretched exponential derived from MD simulations, the average rotational correlation times of the C-D bond on the ring and methyl groups of each probe could be determined.

In the case of the proton axis, recreation of the experimental T_1 values from the fitting program was successful. Comparison of the average rotational correlation times between each probe yielded data that was not expected, specifically for pXy^0 and $DMPy^+$. Despite the opposite interactions with the solvent, the rotational correlation times were nearly identical. With respect to size and shape, pXy^0 and $DMPy^+$ are most closely related, which may account for the

congruent rotational behavior, suggesting that for molecules of this size, charge does not seem to have an effect on rotation. Like the proton observations, the methyl deuteron average rotational correlation times for pXy^0 and $DMPy^+$ were nearly identical over the entire ηT^{-1} range. Though the methyl and proton data do not have identical relationships between the $\langle \tau_{rot} \rangle$ of pXy^0 and $DMPy^+$, both sets of data further support the idea that solute-solvent interactions do not seem to govern the rotational diffusion of the molecules. Unlike the proton data, the methyl deuteron T_1 temperature dependent series suggest that motional narrowing was not achieved, suggesting that further experimental measurements are required.

Appendix: Chemical Shift and T_1 Raw Data

	Branched Cation Diffusion Coefficients (m^2/s)			Linear Cation Diffusion Coefficients (m^2/s)		
n	Trial 1 (19 °C)	Trial 2 (24.5 °C)	Trial 3 (24.5 °C)	Trial 1 (19 °C)	Trial 2 (24.5 °C)	Trial 3 (24.5 °C)
3	3.67E-11	4.13E-11	4.18E-11	4.53E-11	4.40E-11	4.57E-11
4	1.93E-11	2.30E-11	2.34E-11	2.81E-11	2.88E-11	2.86E-11
5	2.11E-11	2.33E-11	2.33E-11	1.86E-11	2.20E-11	2.28E-11
6	1.25E-11	1.65E-11	1.64E-11	1.59E-11	1.95E-11	2.01E-11
7	1.23E-11	1.41E-11	1.41E-11	1.23E-11	1.47E-11	1.48E-11

Table A.1. Branched and linear cation diffusion coefficients measured on the 850 MHz spectrometer.

	Branched Anion Diffusion Coefficients (m^2/s)			Linear Anion Diffusion Coefficients (m^2/s)		
n	Trial 1 (19 °C)	Trial 2 (24.5 °C)	Trial 3 (24.5 °C)	Trial 1 (19 °C)	Trial 2 (24.5 °C)	Trial 3 (24.5 °C)
3	2.80E-11	2.97E-11	2.86E-11	3.43E-11	3.08E-11	3.20E-11
4	1.70E-11	1.79E-11	1.82E-11	2.15E-11	2.14E-11	2.14E-11
5	2.00E-11	2.02E-11	2.04E-11	1.73E-11	1.86E-11	1.94E-11
6	1.47E-11	1.53E-11	1.54E-11	1.62E-11	1.77E-11	1.77E-11
7	1.33E-11	1.34E-11	1.37E-11	1.32E-11	1.37E-11	1.47E-11

Table A.2. Anion diffusion coefficients paired withed branched and linear cations measured on the 850 MHz spectrometer.

Branched Series Chemical Shifts (ppm)

	Trial #1 (360 MHz)					Trial #2 (360 MHz)					Trial #1
n	Term CH3	C2	C4	C5	Im CH3	Term CH3	C2	C4	C5	Im CH3	F
3	1.319	8.354	7.183	7.33	3.686	1.32	8.355	7.184	7.331	3.687	-80.803
4	0.712	8.392	7.223	7.268	3.721	0.711	8.392	7.223	7.267	3.719	-80.690
5	0.74	8.42	7.217	7.312	3.717	0.74	8.42	7.216	7.311	3.715	-80.624
6	0.689	8.44	7.234	7.317	3.734	0.688	8.44	7.234	7.317	3.734	-80.558
7	0.68	8.463	7.248	7.329	3.744	0.679	8.462	7.248	7.328	3.743	-80.536

Linear Series Chemical Shifts (ppm)

	Trial #1 (360 MHz)					Trial #2 (360 MHz)					Trial #1
n	Term CH3	C2	C4	C5	ImCH3	Term CH3	C2	C4	C5	ImCH3	F
3	0.695	8.376	7.206	7.266	3.696	0.702	8.384	7.212	7.272	3.703	-80.8689
4	0.648	8.318	7.149	7.227	3.650	0.663	8.334	7.166	7.245	3.665	-80.8944
5	0.686	8.422	7.234	7.314	3.734	0.695	8.430	7.242	7.322	3.744	-80.730
6	0.682	8.442	7.245	7.324	3.741	0.691	8.457	7.254	7.333	3.753	-80.6752
7	0.706	8.472	7.262	7.342	3.760	0.706	8.471	7.262	7.342	3.760	-80.624
8	0.711	8.468	7.256	7.337	3.754	0.720	8.477	7.265	7.346	3.763	-80.6058

Cation Chemical Shifts of 50 mM IL in DMSO-d (ppm)

	Branched					**Linear**				
n	Term CH3	C2	C4	C5	Im CH3	Term CH3	C2	C4	C5	ImCH3
3	1.472	9.174	7.711	7.873	3.841	0.8577	9.0997	7.7051	7.7617	4.1245
4	0.871	9.088	7.714	7.738	3.861	0.9058	9.1056	7.762	7.6968	3.848
5	0.917	9.125	7.695	7.779	3.846	0.874	9.1055	7.697	7.7662	4.1527

Tables A.3-A.5. Chemical shifts of branched and linear cations in neat liquid and dilute solution.

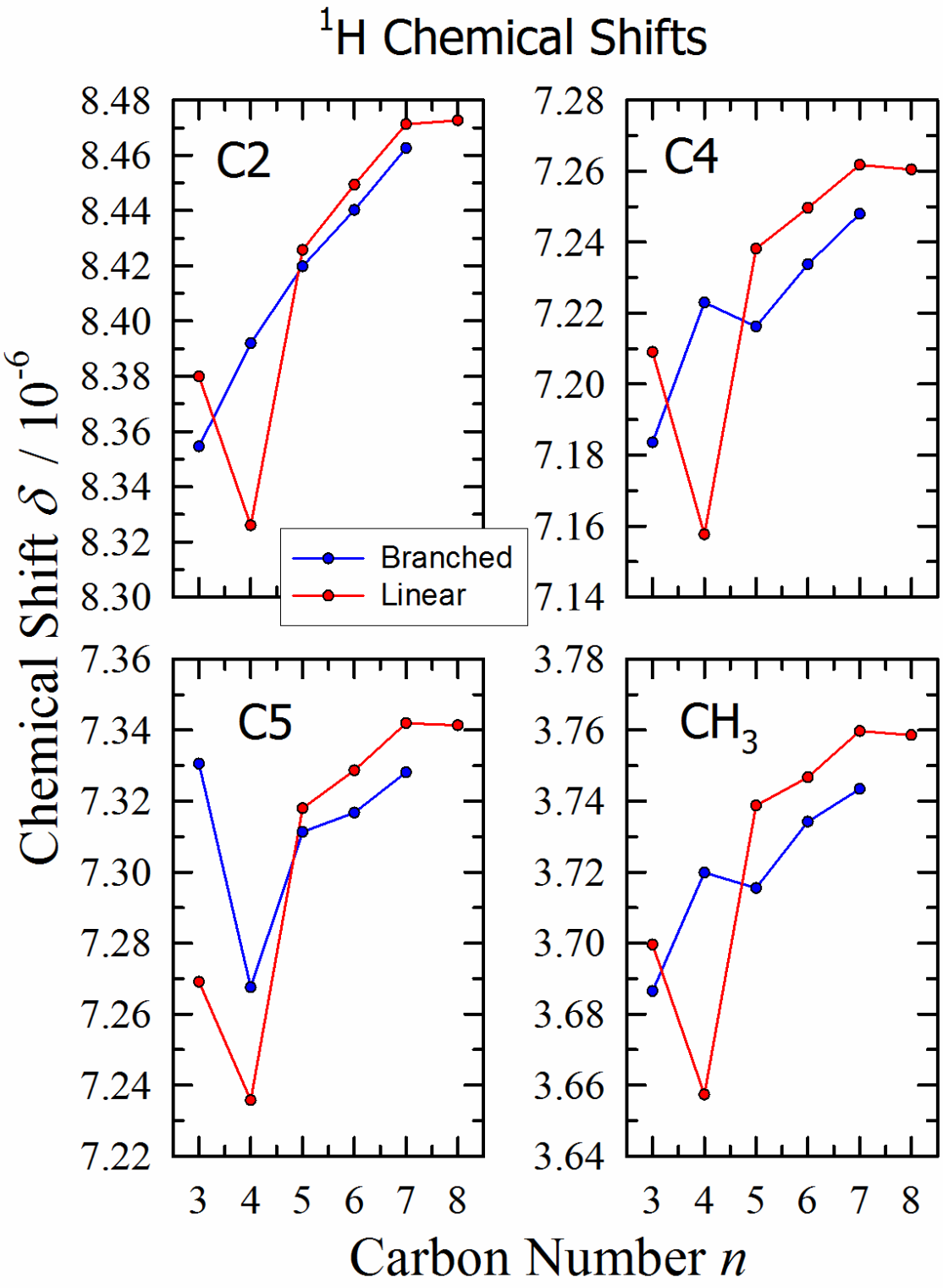

Figure A.1. Chemical shift summary of cation protons in branched (blue) and linear (read) ionic liquids.

[Pyr-d][PF6] 850 MHz T_1 Data

Deuteron	Solvent	T(K)-dial	T(K)-corr	T_1 (s)
CD_3	$[Im_{41}][BF_4]$	358	365.5	1.609
CD_3	$[Im_{41}][BF_4]$	348	354.1	1.425
CD_3	$[Im_{41}][BF_4]$	338	342.8	0.9715
CD_3	$[Im_{41}][BF_4]$	328	331.5	0.7448
CD_3	$[Im_{41}][BF_4]$	318	320.1	0.4821
CD_3	$[Im_{41}][BF_4]$	308	308.8	0.2526
CD_3	$[Im_{41}][BF_4]$	298	297.6	0.1665
CD_3	$[Im_{41}][BF_4]$	283	285.2	0.1400
CD_3	$[Im_{41}][BF_4]$	273	277.0	0.1710
CD_3	CH_3CN	298	297.6	0.0267
D (ortho CH3)	$[Im_{41}][BF_4]$	358	365.5	0.1951
D (ortho CH3)	$[Im_{41}][BF_4]$	348	354.1	0.1456
D (ortho CH3)	$[Im_{41}][BF_4]$	338	342.8	0.1110
D (ortho CH3)	$[Im_{41}][BF_4]$	328	331.5	0.0817
D (ortho CH3)	$[Im_{41}][BF_4]$	318	320.1	0.0601
D (ortho CH3)	$[Im_{41}][BF_4]$	308	308.8	0.0377
D (ortho CH3)	$[Im_{41}][BF_4]$	298	297.6	0.0235
D (ortho CH3)	$[Im_{41}][BF_4]$	283	285.2	0.0107
D (ortho CH3)	$[Im_{41}][BF_4]$	273	277.0	0.0126
D (ortho CH3)	CH_3CN	298	297.6	0.5587
D (meta CH3)	$[Im_{41}][BF_4]$	358	365.5	0.1894
D (meta CH3)	$[Im_{41}][BF_4]$	348	354.1	0.1574
D (meta CH3)	$[Im_{41}][BF_4]$	338	342.8	0.1144
D (meta CH3)	$[Im_{41}][BF_4]$	328	331.5	0.0895
D (meta CH3)	$[Im_{41}][BF_4]$	318	320.1	0.0539
D (meta CH3)	$[Im_{41}][BF_4]$	308	308.8	0.0354
D (meta CH3)	$[Im_{41}][BF_4]$	298	297.6	0.0238
D (meta CH3)	$[Im_{41}][BF_4]$	283	285.2	0.0110
D (meta CH3)	$[Im_{41}][BF_4]$	273	277.0	0.0129
D (meta CH3)	CH_3CN	298	297.6	0.5406

Table A.6. *T_1* data for $DMPy^+$ on the 850 MHz spectrometer.

[Pyr-d][PF6] 300 MHz T_1 Data

Deuteron	Solvent	T(K)-dial	T(K)-corr	T_1 (s)
CD_3	$[Im_{41}][BF_4]$	333	337.1	0.6016
CD_3	$[Im_{41}][BF_4]$	328	331.5	0.4753
CD_3	$[Im_{41}][BF_4]$	323	325.8	0.3840
CD_3	$[Im_{41}][BF_4]$	318	320.1	0.3087
CD_3	$[Im_{41}][BF_4]$	313	314.5	0.2795
CD_3	$[Im_{41}][BF_4]$	308	308.8	0.2217
CD_3	$[Im_{41}][BF_4]$	298	297.4	0.1460
CD_3	$[Im_{41}][BF_4]$	283	280.4	0.0488
CD_3	$[Im_{41}][BF_4]$	273	275.0	0.0406
CD_3	$[Im_{41}][BF_4]$	268	269.8	0.0389
CD_3	$[Im_{41}][BF_4]$	263	263.5	0.0372
CD_3	$[Im_{41}][BF_4]$	258	258.2	0.0403
D (ortho CH_3)	$[Im_{41}][BF_4]$	333	337.1	0.0861
D (ortho CH_3)	$[Im_{41}][BF_4]$	328	331.5	0.0731
D (ortho CH_3)	$[Im_{41}][BF_4]$	323	325.8	0.0595
D (ortho CH_3)	$[Im_{41}][BF_4]$	318	320.1	0.0520
D (ortho CH_3)	$[Im_{41}][BF_4]$	313	314.5	0.0452
D (ortho CH_3)	$[Im_{41}][BF_4]$	308	308.8	0.0347
D (ortho CH_3)	$[Im_{41}][BF_4]$	298	297.4	0.0225
D (ortho CH_3)	$[Im_{41}][BF_4]$	283	280.4	0.0085
D (ortho CH_3)	$[Im_{41}][BF_4]$	273	275.0	0.0053
D (ortho CH_3)	$[Im_{41}][BF_4]$	268	269.8	0.0048
D (ortho CH_3)	$[Im_{41}][BF_4]$	263	263.5	0.0040
D (ortho CH_3)	$[Im_{41}][BF_4]$	258	258.2	0.0037
D (meta CH_3)	$[Im_{41}][BF_4]$	333	337.1	0.0939
D (meta CH_3)	$[Im_{41}][BF_4]$	328	331.5	0.0756
D (meta CH_3)	$[Im_{41}][BF_4]$	323	325.8	0.0612
D (meta CH_3)	$[Im_{41}][BF_4]$	318	320.1	0.0513
D (meta CH_3)	$[Im_{41}][BF_4]$	313	314.5	0.0456
D (meta CH_3)	$[Im_{41}][BF_4]$	308	308.8	0.0355
D (meta CH_3)	$[Im_{41}][BF_4]$	298	297.4	0.0227
D (meta CH_3)	$[Im_{41}][BF_4]$	283	280.4	0.0083
D (meta CH_3)	$[Im_{41}][BF_4]$	273	275.0	0.0053
D (meta CH_3)	$[Im_{41}][BF_4]$	268	269.8	0.0048
D (meta CH_3)	$[Im_{41}][BF_4]$	263	263.5	0.0040
D (meta CH_3)	$[Im_{41}][BF_4]$	258	258.2	0.0037

Table A.7. T_1 data for $DMPy^+$ on the 300 MHz spectrometer.

p-xylene-d10 850 MHz T_1 Data

Deuteron	Solvent	T(K)-dial	T(K)-corr	T_1 (s)
CD_3	$[Im_{41}][BF_4]$	358	365.5	1.869
CD_3	$[Im_{41}][BF_4]$	348	354.1	1.200
CD_3	$[Im_{41}][BF_4]$	338	342.8	0.983
CD_3	$[Im_{41}][BF_4]$	328	331.5	0.6906
CD_3	$[Im_{41}][BF_4]$	318	320.1	0.4519
CD_3	$[Im_{41}][BF_4]$	308	308.8	0.2942
CD_3	$[Im_{41}][BF_4]$	298	297.6	0.2040
CD_3	$[Im_{41}][BF_4]$	283	285.2	0.1449
CD_3	$[Im_{41}][BF_4]$	273	277.0	0.1465
CD_3	CH_3CN	298	297.6	3.664
D	$[Im_{41}][BF_4]$	358	365.5	0.1824
D	$[Im_{41}][BF_4]$	348	354.1	0.1364
D	$[Im_{41}][BF_4]$	338	342.8	0.1016
D	$[Im_{41}][BF_4]$	328	331.5	0.0683
D	$[Im_{41}][BF_4]$	318	320.1	0.0461
D	$[Im_{41}][BF_4]$	308	308.8	0.0292
D	$[Im_{41}][BF_4]$	298	297.6	0.0193
D	$[Im_{41}][BF_4]$	283	285.2	0.0119
D	$[Im_{41}][BF_4]$	273	277.0	0.0120
D	CH_3CN	298	297.6	0.7527

Table A.8. T_1 data for pXy^0 on the 850 MHz spectrometer.

p-xylene-d10 300 MHz T_1 Data

Deuteron	Solvent	T(K)-dial	T(K)-corr	T_1 (s)
CD_3	$[Im_{41}][BF_4]$	333	337.1	0.5852
CD_3	$[Im_{41}][BF_4]$	328	331.5	0.5257
CD_3	$[Im_{41}][BF_4]$	323	325.8	0.4447
CD_3	$[Im_{41}][BF_4]$	318	320.1	0.3710
CD_3	$[Im_{41}][BF_4]$	313	314.5	0.3041
CD_3	$[Im_{41}][BF_4]$	308	308.8	0.2398
CD_3	$[Im_{41}][BF_4]$	298	297.4	0.1492
CD_3	$[Im_{41}][BF_4]$	283	280.4	0.0694
CD_3	$[Im_{41}][BF_4]$	273	275.0	0.0529
CD_3	$[Im_{41}][BF_4]$	268	269.8	0.0519
CD_3	$[Im_{41}][BF_4]$	263	263.5	0.0526
CD_3	$[Im_{41}][BF_4]$	258	258.2	0.0605
CD_3	$[Im_{41}][BF_4]$	243	243.6	0.0732
D	$[Im_{41}][BF_4]$	333	337.1	0.0805
D	$[Im_{41}][BF_4]$	328	331.5	0.0681
D	$[Im_{41}][BF_4]$	323	325.8	0.0585
D	$[Im_{41}][BF_4]$	318	320.1	0.0465
D	$[Im_{41}][BF_4]$	313	314.5	0.0375
D	$[Im_{41}][BF_4]$	308	308.8	0.0294
D	$[Im_{41}][BF_4]$	298	297.4	0.0178
D	$[Im_{41}][BF_4]$	283	280.4	0.0079
D	$[Im_{41}][BF_4]$	273	275.0	0.0067
D	$[Im_{41}][BF_4]$	268	269.8	0.0061
D	$[Im_{41}][BF_4]$	263	263.5	0.0054
D	$[Im_{41}][BF_4]$	258	258.2	0.0063
D	$[Im_{41}][BF_4]$	243	243.6	0.0077

Table A.9. *T_1* data for pXy^0 on the 300 MHz spectrometer.

p-tolunitrile-d7 850 MHz T_1 Data

Deuteron	Solvent	T(K)-dial	T(K)-corr	T_1 (s)
CD_3	$[Im_{41}][BF_4]$	358	365.5	0.8360
CD_3	$[Im_{41}][BF_4]$	348	354.1	0.6000
CD_3	$[Im_{41}][BF_4]$	338	342.8	0.4606
CD_3	$[Im_{41}][BF_4]$	328	331.5	0.2713
CD_3	$[Im_{41}][BF_4]$	318	320.1	0.2129
CD_3	$[Im_{41}][BF_4]$	308	308.8	0.1364
CD_3	$[Im_{41}][BF_4]$	298	297.6	0.1338
D (ortho CH_3)	$[Im_{41}][BF_4]$	358	365.5	0.0957
D (ortho CH_3)	$[Im_{41}][BF_4]$	348	354.1	0.07099
D (ortho CH_3)	$[Im_{41}][BF_4]$	338	342.8	0.04887
D (ortho CH_3)	$[Im_{41}][BF_4]$	328	331.5	0.03288
D (ortho CH_3)	$[Im_{41}][BF_4]$	318	320.1	0.02507
D (ortho CH_3)	$[Im_{41}][BF_4]$	308	308.8	0.01526
D (ortho CH_3)	$[Im_{41}][BF_4]$	298	297.6	0.01055
D (meta CH_3)	$[Im_{41}][BF_4]$	358	365.5	0.0957
D (meta CH_3)	$[Im_{41}][BF_4]$	348	354.1	0.07099
D (meta CH_3)	$[Im_{41}][BF_4]$	338	342.8	0.04887
D (meta CH_3)	$[Im_{41}][BF_4]$	328	331.5	0.03288
D (meta CH_3)	$[Im_{41}][BF_4]$	318	320.1	0.02507
D (meta CH_3)	$[Im_{41}][BF_4]$	308	308.8	0.01526
D (meta CH_3)	$[Im_{41}][BF_4]$	298	297.6	0.01055

Table A.10. T_1 data for $CMBz^{\mu}$ on the 850 MHz spectrometer.

p-tolunitrile-d7 300 MHz T_1 Data

Deuteron	Solvent	T(K)-dial	T(K)-corr	T_1 (s)
CD_3	$[Im_{41}][BF_4]$	358	337.1	0.5760
CD_3	$[Im_{41}][BF_4]$	348	331.5	0.4421
CD_3	$[Im_{41}][BF_4]$	338	325.8	0.3472
CD_3	$[Im_{41}][BF_4]$	328	320.1	0.2502
CD_3	$[Im_{41}][BF_4]$	318	314.5	0.1708
CD_3	$[Im_{41}][BF_4]$	308	308.8	0.0994
CD_3	$[Im_{41}][BF_4]$	298	297.4	0.0618
CD_3	$[Im_{41}][BF_4]$	283	280.4	0.03622
CD_3	$[Im_{41}][BF_4]$	273	275.0	0.03681
CD_3	$[Im_{41}][BF_4]$	268	269.8	0.04078
CD_3	$[Im_{41}][BF_4]$	263	264.5	0.05004
D (ortho CH_3)	$[Im_{41}][BF_4]$	358	337.1	0.09187
D (ortho CH_3)	$[Im_{41}][BF_4]$	348	331.5	0.06999
D (ortho CH_3)	$[Im_{41}][BF_4]$	338	325.8	0.05
D (ortho CH_3)	$[Im_{41}][BF_4]$	328	320.1	0.03521
D (ortho CH_3)	$[Im_{41}][BF_4]$	318	314.5	0.02233
D (ortho CH_3)	$[Im_{41}][BF_4]$	308	308.8	0.01384
D (ortho CH_3)	$[Im_{41}][BF_4]$	298	297.4	0.008442
D (ortho CH_3)	$[Im_{41}][BF_4]$	283	280.4	0.004137
D (ortho CH_3)	$[Im_{41}][BF_4]$	273	275.0	0.004989
D (ortho CH_3)	$[Im_{41}][BF_4]$	268	269.8	0.005589
D (ortho CH_3)	$[Im_{41}][BF_4]$	263	264.5	0.005786
D (meta CH_3)	$[Im_{41}][BF_4]$	358	337.1	0.09434
D (meta CH_3)	$[Im_{41}][BF_4]$	348	331.5	0.06859
D (meta CH_3)	$[Im_{41}][BF_4]$	338	325.8	0.05055
D (meta CH_3)	$[Im_{41}][BF_4]$	328	320.1	0.0353
D (meta CH_3)	$[Im_{41}][BF_4]$	318	314.5	0.02272
D (meta CH_3)	$[Im_{41}][BF_4]$	308	308.8	0.01384
D (meta CH_3)	$[Im_{41}][BF_4]$	298	297.4	0.008442
D (meta CH_3)	$[Im_{41}][BF_4]$	283	280.4	0.004137
D (meta CH_3)	$[Im_{41}][BF_4]$	273	275.0	0.004989
D (meta CH_3)	$[Im_{41}][BF_4]$	268	269.8	0.005589
D (meta CH_3)	$[Im_{41}][BF_4]$	263	264.5	0.005786

Table A.11. *T_1* data for $CMBz^{\mu}$ on the 300 MHz spectrometer.

References

1. Kaintz, A.; Baker, G.; Benesi, A.; Maroncelli, M., Solute Diffusion in Ionic Liquids, NMR Measurements and Comparisons to Conventional Solvents. *The Journal of Physical Chemistry B* 2013, *117* (39), 11697-11708.

2. (a) Kaintz, A. E. Translational And Rotational Diffusion in Ionic Liquids. Ph. D., The Pennsylvania State University, State College, Pennsylvania, 2013; (b) Xue, L. B., Fehmi; Tamas, George; Gurung, Eshan; Koh, Yung P.; Simon, Sindee L; Quitevis, Edward L., Comparative Study of the OKE Spectra and Phyiscal Properties of Branched and Linear Alkyl Chain Imidazolium Ionic Liquids. Texas Tech University: Lubbock, Texas, 2013.

3. (a) Zigah, D.; Ghilane, J.; Lagrost, C.; Hapiot, P., Variations of Diffusion Coefficients of Redox Active Molecules in Room Temperature Ionic Liquids upon Electron Transfer. *The Journal of Physical Chemistry B* 2008, *112* (47), 14952-14958; (b) Ghilane, J.; Lagrost, C.; Hapiot, P., Scanning Electrochemical Microscopy in Nonusual Solvents: Inequality of Diffusion Coefficients Problem. *Anal. Chem.* 2007, *79* (19), 7383-7391; (c) Evans, R. G.; Klymenko, O. V.; Hardacre, C.; Seddon, K. R.; Compton, R. G., Oxidation of N,N,N′,N′-tetraalkyl-para-phenylenediamines in a series of room temperature ionic liquids incorporating the bis(trifluoromethylsulfonyl)imide anion. *J. Electroanal. Chem.* 2003, *556* (0), 179-188; (d) Xiong, L.; Aldous, L.; Henstridge, M. C.; Compton, R. G., Investigation of the optimal transient times for chronoamperometric analysis of diffusion coefficients and concentrations in non-aqueous solvents and ionic liquids. *Analytical Methods* 2012, *4* (2), 371-376; (e) Zistler, M. W., Philipp; Schreiner, Christian; Gores, Heiner J., Electrochemical of triiodide diffusion coefficients in blends of ionic liquids Results for improving a critical parameter of dye-sensitized solar cells. *J. Mol. Liq.* 2010, *156* (1), 52-57; (f) Zistler, M.; Wachter, P.; Wasserscheid, P.; Gerhard, D.; Hinsch, A.; Sastrawan, R.; Gores, H. J., Comparison of electrochemical methods for triiodide diffusion coefficient measurements and observation of non-Stokesian diffusion behaviour in binary mixtures of two ionic liquids. *Electrochim. Acta* 2006, *52* (1), 161-169; (g) Shoup, D.; Szabo, A., Chronoamperometric current at finite disk electrodes. *Journal of Electroanalytical Chemistry and Interfacial Electrochemistry* 1982, *140* (2), 237-245.

4. (a) Jin, H.; Baker, G. A.; Arzhantsev, S.; Dong, J.; Maroncelli, M., Solvation and Rotational Dynamics of Coumarin 153 in Ionic Liquids: Comparisons to Conventional Solvents. *The Journal of Physical Chemistry B* 2007, *111* (25), 7291-7302; (b) Karve, L.; Dutt, G. B., Rotational Diffusion of Neutral and Charged Solutes in 1-Butyl-3-Methylimidazolium-Based Ionic Liquids: Influence of the Nature of the Anion on Solute Rotation. *The Journal of Physical Chemistry B* 2012, *116* (6), 1824-1830; (c) Mladenova, B. Y.; Chumakova, N. A.; Pergushov, V. I.; Kokorin, A. I.; Grampp, G.; Kattnig, D. R., Rotational and Translational Diffusion of Spin Probes in Room-Temperature Ionic Liquids. *The Journal of Physical Chemistry B* 2012, *116* (40), 12295-12305; (d) Strehmel, V.; Berdzinski, S.; Rexhausen, H., Interactions between ionic liquids and radicals. *J. Mol. Liq.* 2014, *192* (0), 153-170; (e) Gangamallaiah, V.; Dutt, G. B., Influence of the Organized Structure of 1-Alkyl-3-Methylimidazolium-Based Ionic Liquids on the Rotational Diffusion of an Ionic Solute. *The Journal of Physical Chemistry B* 2013, *117* (34), 9973-9979.

5. Levitt, M. H., *Spin Dynamics: Basics of Nuclear Magnetic Resonance*. John Wiley & Sons, Ltd.: New York, 2001.

6. (a) Yasaka, Y.; Wakai, C.; Matubayasi, N.; Nakahara, M., Rotational dynamics of water and benzene controlled by anion field in ionic liquids: 1-butyl-3-methylimidazolium chloride and hexafluorophosphate. *The Journal of Chemical Physics* 2007, *127* (10), 104506; (b) Yasaka, Y.; Klein, M. L.; Nakahara, M.; Matubayasi, N., Rotational dynamics of benzene and water in an ionic liquid explored via molecular dynamics simulations and NMR T1 measurements. *The Journal of Chemical Physics* 2012, *136* (7), 074508.

7. (a) Wahlbeck, P. G.; Carper, W. R., SEPARATION OF 13C NMR RELAXATION MECHANISMS IN VISCOUS SOLUTIONS. *Chem. Eng. Commun.* 2007, *194* (9), 1160-1168; (b) Alam, T. M.; Dreyer, D. R.; Bielwaski, C. W.; Ruoff, R. S., Measuring Molecular Dynamics and Activation Energies for Quaternary Acyclic Ammonium and Cyclic Pyrrolidinium Ionic Liquids Using 14N NMR Spectroscopy. *The Journal of Physical Chemistry A* 2011, *115* (17), 4307-4316; (c) Carper, W. R.; Wahlbeck, P. G.; Dölle, A., 13C NMR Relaxation Rates: Separation of Dipolar and Chemical Shift Anisotropy Effects. *The Journal of Physical Chemistry A* 2004, *108* (29), 6096-6099; (d) Antony, J. H.; Dölle, A.; Mertens, D.; Wasserscheid, P.; Carper, W. R.; Wahlbeck, P. G., 13C NMR Relaxation Rates in the Ionic Liquid 1-Methyl-3-nonylimidazolium Hexafluorophosphate. *The Journal of Physical Chemistry A* 2005, *109* (30), 6676-6682; (e) Matveev, V. V.; Markelov, D. A.; Brui, E. A.; Chizhik, V. I.; Ingman, P.; Lahderanta, E., 13C NMR relaxation and reorientation dynamics in imidazolium-based ionic liquids: revising interpretation. *PCCP* 2014, *16* (22), 10480-10484.

8. Raiford, D. S.; Fisk, C. L.; Becker, E. D., Calibration of methanol and ethylene glycol nuclear magnetic resonance thermometers. *Anal. Chem.* 1979, *51* (12), 2050-2051.

9. Araque, J. C.; Yadav, S. K.; Shadeck, M.; Maroncelli, M.; Margulis, C. J., How Is Diffusion of Neutral and Charged Tracers Related to the Structure and Dynamics of a Room-Temperature Ionic Liquid? Large Deviations from Stokes–Einstein Behavior Explained. *The Journal of Physical Chemistry B* 2015.

10. (a) Lipari, G.; Szabo, A., Model-free approach to the interpretation of nuclear magnetic resonance relaxation in macromolecules. 2. Analysis of experimental results. *J. Am. Chem. Soc.* 1982, *104* (17), 4559-4570; (b) Lipari, G.; Szabo, A., Model-free approach to the interpretation of nuclear magnetic resonance relaxation in macromolecules. 1. Theory and range of validity. *J. Am. Chem. Soc.* 1982, *104* (17), 4546-4559.